Article

Current Biology

Membrane Curvature Catalyzes Lipid Droplet Assembly

Highlights

- The presence of free TG molecules is unfavorable in curved membranes
- Membrane curvature facilitates but sterol esters inhibit the assembly of TG LDs
- Endoplasmic reticulum topology modulates the number of assembled LDs
- Seipin controls the condensation of TGs into LDs at endoplasmic reticulum tubules

Authors

Alexandre Santinho, Veijo T. Salo, Aymeric Chorlay, ..., Mohyeddine Omrane, Elina Ikonen, Abdou Rachid Thiam

Correspondence

thiam@ens.fr

In Brief

How triglycerides (TGs) in the ER bilayer condense into lipid droplets (LDs) is poorly known. Santinho et al. show that membrane curvature aids this transition by reducing the critical TG concentration needed for condensing into LDs. Seipin is enriched at tubules and controls this condensation step, preventing uncontrolled LD assembly at ER tubules.

Santinho et al., 2020, Current Biology *30*, 2481–2494
July 6, 2020
https://doi.org/10.1016/j.cub.2020.04.066

CellPress

Current Biology

CellPress

Article

Membrane Curvature Catalyzes Lipid Droplet Assembly

Alexandre Santinho,[1] Veijo T. Salo,[2,3] Aymeric Chorlay,[1] Shiqian Li,[2,3] Xin Zhou,[2,3] Mohyeddine Omrane,[1] Elina Ikonen,[2,3] and Abdou Rachid Thiam[1,4,*]

[1]Laboratoire de Physique de l'École Normale Supérieure, ENS, Université PSL, CNRS, Sorbonne Université, Université de Paris, 75005 Paris, France

[2]Department of Anatomy and Stem Cells and Metabolism Research Program, Faculty of Medicine, University of Helsinki, 00290 Helsinki, Finland

[3]Minerva Foundation Institute for Medical Research, 00290 Helsinki, Finland

[4]Lead Contact

*Correspondence: thiam@ens.fr

https://doi.org/10.1016/j.cub.2020.04.066

SUMMARY

Lipid droplet (LD) biogenesis begins in the endoplasmic reticulum (ER) bilayer, but how the ER topology impacts this process is unclear. An early step in LD formation is nucleation, wherein free neutral lipids, mainly triacylglycerols (TGs) and sterol esters (SEs), condense into a nascent LD. How this transition occurs is poorly known. Here, we found that LDs preferably assemble at ER tubules, with higher curvature than ER sheets, independently of the LD assembly protein seipin. Indeed, the critical TG concentration required for initiating LD assembly is lower at curved versus flat membrane regions. In agreement with this finding, flat ER regions bear higher amounts of free TGs than tubular ones and present less LDs. By using an *in vitro* approach, we discovered that the presence of free TGs in tubules is energetically unfavorable, leading to outflow of TGs to flat membrane regions or condensation into LDs. Accordingly, *in vitro* LD nucleation can be achieved by the sole increase of membrane curvature. In contrast to TGs, the presence of free SEs is favored at tubules and increasing SE levels is inhibitory to the curvature-induced nucleation of TG LDs. Finally, we found that seipin is enriched at ER tubules and controls the condensation process, preventing excessive tubule-induced nucleation. The absence of seipin provokes erratic LD nucleation events determined by the abundance of ER tubules. In summary, our data indicate that membrane curvature catalyzes LD assembly.

INTRODUCTION

Lipid droplets (LDs) are organelles at the center of cellular energy metabolism [1]. LDs consist of a neutral lipid (NL) oil core, mainly composed of triacylglycerols (TGs) and/or sterol esters (SEs), covered by a phospholipid (PL) monolayer containing proteins.

The biogenesis of LDs is triggered under various physiological conditions and proceeds via successive biochemical and biophysical reactions taking place at the endoplasmic reticulum (ER) [2, 3]. During conditions favoring lipid storage, these biochemical reactions mediate NL synthesis. NL oil molecules are encapsulated between the ER bilayer leaflets due to their hydrophobicity and diffuse within the ER. When a critical concentration of NLs is reached, the molecules phase separate from the PL bilayer and assemble into stabilized condensed structures [4]. This condensation and phase separation process, predicted by molecular dynamic simulations [5, 6], is termed nucleation [7]. The NL condensate forms a nascent LD that grows and buds into the cytosol [3, 8]. This emergence of a LD from the ER bilayer is influenced by several membrane physicochemical properties, such as PL composition, tension, and shape, as well as proteins bound to the surface of the forming LD [5, 9]. For example, higher membrane surface tension, altered by PLs or membrane shape, impedes LD assembly and promotes large LDs [5]; membrane curvature and the recruitment of proteins or PLs to the outer ER membrane leaflet favor external LD emergence [9–11]. However, how these factors impact on LD nucleation, i.e., LD assembly initiation, remains poorly understood. This is because nucleation happens at nanometric scales, making it difficult to investigate.

NLs condense in a bilayer when they reach a critical concentration [5, 6, 12]. This concentration is coupled to an energy barrier that depends on factors such as protein-lipid and lipid-lipid interactions and membrane topology, such as curvature [7]. Topologically, the ER bilayer is made of sheets and tubules, whose relative abundance is affected by the cell type and phase [13]. Interestingly, LDs made of different NLs may arise at precise ER subregions [14–17]. It is currently unknown whether the ER topology and composition affect LD nucleation.

Although many proteins affect the size and number of LDs, no single protein appears indispensable for LD formation. This is likely because NLs may behave as confined fluids that can spontaneously condense into droplets [7]. However, it is crucial for cells to control such a condensation process to regulate LD assembly. A key protein implicated in LD assembly is seipin [18, 19]. It is an oligomeric ER membrane protein [20–22] whose dysfunction is linked to severe forms of lipodystrophy [23] and neurological diseases [24, 25]. Seipin oligomers are motile in

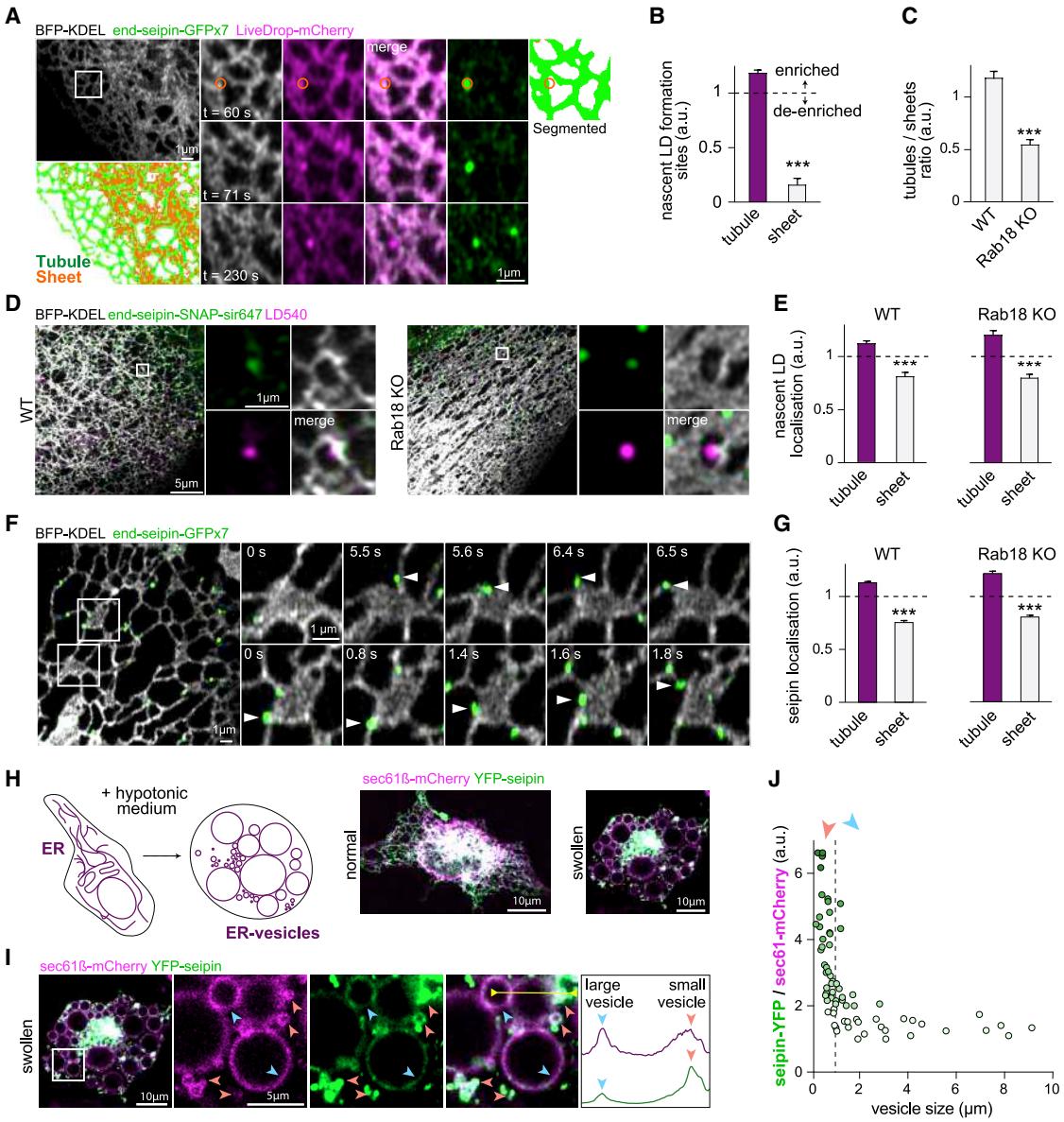

Figure 1. LDs Are Generated at ER Tubules Where Seipin Is Enriched

(A) A431 cells with seipin tagged endogenously with GFPx7 (end-seipin-GFPx7) and stably expressing BFP-KDEL and LiveDrop-mCherry were delipidated (1 day LPDS) and imaged live with Airyscan microscopy, starting 50 s after OA loading. ER tubules and sheets were segmented as described in STAR Methods. Insets show an example of an emerging LD, and circle denotes region of interest (ROI) marked by seipin, used for analysis in (B).

(B) Analysis of nascent LD formation sites from (A); the distribution of segmented ER pixels at LD-associated seipin foci prior to LiveDrop accumulation was analyzed and compared to overall pixel distribution of sheets/tubules in the same cells. Bars: mean ± SEM, n = 26 LDs, 6 cells, 2 experiments.

(C) WT and Rab 18 KO cells stably expressing BFP-KDEL cells were imaged live, and the ER was segmented and analyzed. Bars: mean ± SEM, n = 54–61 ROIs from 54–61 cells/genotype, 3 experiments.

(D) A431 WT and Rab18 KO cells with seipin tagged endogenously with SNAPf-tag and stably expressing BFP-KDEL were delipidated (3 days LPDS; 18 h DGATi), and seipin was stained with SIR647 4–6 h prior to imaging. After DGATi washout, OA, SOAT1 inhibitor, and LD540 were added to the cells, and they were imaged live 0–15 min after OA addition.

(E) Analysis of (D). The distribution of segmented ER pixels at LD-associated seipin foci was compared to overall pixel distribution of sheets/tubules in the same cells. Bars: mean ± SEM, n = 25–38 ROIs from 25–38 cells, 2 to 3 experiments (>800 LD-associated seipins/genotype).

(F) End-seipin-GFPx7 cells stably expressing BFP-KDEL were imaged live. Seipin is enriched at ER tubules and, when moving through sheet regions (insets), prefers the edges of sheets.

(G) Analysis of (D). The distribution of segmented ER pixels at each seipin ROI was compared to overall pixel distribution of sheets/tubules in the same cells. Bars: mean ± SEM, n = 25–38 ROIs from 25–38 cells, 2 to 3 experiments (>9,000 seipin foci/genotype).

(H) Schematic representation of the ER vesicles formation with swollen cells. Left: Cos7 cell expressing sec61β-mCherry and YFP-seipin was imaged live by confocal microscopy. Right: Cos7 cell expressing sec61β-mCherry and YFP-seipin was imaged live 10 min after ER vesicle formation.

(legend continued on next page)

the ER and arrest at sites where LDs emerge [26, 27]. At these sites, seipin is able to promote the growth of the newborn LDs and prevent their shrinkage by Ostwald ripening [7, 28]. How seipin acts in this process is still unclear, but it might transfer TGs into forming LDs [21, 28] and/or modulate the local PL milieu [2, 22, 29]. In the absence of seipin, a phenotype of few supersized and many tiny LDs appears [18, 26, 27]. This tiny LD population is reduced by the concomitant depletion of Rab18 [28], another organizer of LD assembly [30].

Here, we found that the ER membrane curvature catalyzes LD assembly and LDs form at ER tubules. However, free TGs do not favor highly curved bilayers per se. Rather, curvature increases the chemical potential of TGs, and upon increasing TG concentration in tubules, phase separation into LDs is triggered. Seipin is enriched at tubules, controlling LD assembly and facilitating TG flux to LDs. By this mechanism, seipin keeps the free TG level in the ER below a critical nucleation concentration, thereby preventing uncontrolled nucleation. Indeed, without seipin, erratic nucleation events occur, controlled by the abundance of ER tubules.

RESULTS

ER Tubules Are the Sites of LD Assembly and Enriched in Seipin

We previously reported that upon oleic acid (OA) administration to human A431 cells, LDs start to develop at ER domains marked by seipin [28]. Indeed, in these cells, nascent LDs, visualized by the LD targeted model peptide LiveDrop-mCherry, appear at sites marked by endogenously fluorescently tagged seipin (Figure 1A). Several studies have suggested ER tubules as the birthplace for LDs [31, 32], but this has not been systematically investigated and the underlying principles remain unknown.

To investigate the relationship between LD formation and ER morphology, we utilized the machine-learning-based image analysis software ilastik to discern ER sheets and tubules from Airyscan live-cell images of the ER visualized by the fluorescent ER marker BFP-KDEL. Using this analysis, we found that the sites of LD formation marked by seipin were highly enriched at ER tubules (Figures 1A and 1B). Of note, our ER segmentation method recapitulated the previously documented enrichment of known ER subdomain marker proteins at sheets or tubules (Figures S1A–S1C) [33, 34]. As a further validation of the analysis tool, we analyzed the ER morphology in control and Rab18 knockout (KO) cells. Rab18 KO has been reported to expand ER sheets at the expense of tubules in Cos7 cells [35], and a similar phenotype was found in A431 cells (Figure 1C). Because Rab18 KO strongly reversed the tubule-to-sheet ratio (Figure 1C), we examined the sites of LD formation under this condition as compared to wild type (WT). To this end, we stringently delipidated the cells and then induced LD biogenesis by addition of OA, imaging cells during the first 15 min of LD biogenesis. We analyzed the localization of LDs marked by the NL dye LD540 and LD-associated seipins. Nascent LDs were enriched at ER tubules in both WT and Rab18 KO cells, despite the higher fraction of sheets in Rab18 KO cells (Figures 1D and 1E).

As seipin can determine the site of LD formation [28] and LDs appeared to preferentially assemble at ER tubules, we investigated the localization of seipin in the ER. In live-cell video recordings, seipin foci were highly motile in the ER, as previously reported [26, 27]. Often, when traveling via a sheet-like region, seipin appeared to move along the edges of the sheet (Figure 1F), barely scanning the planar surface. Image analysis revealed seipin to be enriched at ER tubules (Figure 1G). This enrichment was also apparent in Rab18 KO cells (Figure 1G), even though these cells harbored less ER tubules (Figure 1C).

To further investigate the localization of seipin in relation to membrane curvature, we induced the formation of large intracellular ER-derived vesicles by adding a hypotonic culture medium to the cells (Figures 1H, 1I, and S1E) [36, 37]. We worked with Cos7 cells transfected with sec61β-mCherry and mouse YFP-seipin, which colocalized (Figures 1H and S1D). We observed the formation of numerous ER vesicles of heterogeneous sizes, larger vesicles with lower curvature and smaller vesicles with higher curvature, decorated by sec61β-mCherry (Figures 1H, 1I, and S1E). We also captured situations where ER vesicles co-existed with tubular structures (Figure S1F). In this system, we found that the YFP-seipin signal was more intense on smaller ER vesicles (Figures 1I and S1E) and tubules (Figure S1F) than on large ER vesicles. By comparing the ratio of seipin to sec61β signal, we observed an enrichment of seipin in smaller ER vesicles (Figure 1J). Similar results were obtained in HeLa cells (Figures S1G and S1H). These data suggest that seipin prefers regions of the ER with a higher curvature and may act as a curvature sensor or inducer, or be associated with one.

Overall, these data show that LD assembly is initiated at ER tubules, even when the tubular fraction is markedly decreased by Rab18 KO. Seipin is enriched at curved regions and may function as a nucleator of LDs at ER tubules.

LDs Also Nucleate at Tubules in the Absence of Seipin

If seipin nucleates LDs at tubules, its depletion might alter this tubule-dependent nucleation of LDs. We thus investigated the sites of LD biogenesis in the absence of seipin. We used seipin-degron cells where seipin can be inducibly and rapidly depleted by the administration of indole acetic acid (IAA) [28]. IAA pretreated seipin degron cells display dramatically altered LD formation, with a high number of tiny LDs and some supersized LDs appearing upon OA treatment [28]. Remarkably, even in the absence of seipin, nascent LDs were enriched at ER tubules (Figures 2A and 2B). In both the absence and presence of seipin, this enrichment at ER tubules was more evident for smaller, apparently younger LDs (Figures S2A and S2B).

To further study the contribution of curvature and seipin in LD nucleation, we took advantage of the heterogeneity of curvature in the ER-derived vesicles and probed LD assembly sites in this

(I) Cos7 cells expressing sec61β-mCherry and YFP-seipin were imaged live 10 min after ER-vesicle formation. Submicrometric ER vesicles (red arrows) display brighter YFP-seipin signal than larger vesicles (blue arrows). Line scan over two ER vesicles (yellow line) displays brighter signal for the small vesicle.
(J) Analysis of (I). The fluorescence intensity ratio of YFP-seipin and sec61β-mCherry is plotted relative to vesicle size, indicating seipin is enriched on submicrometric vesicles, n = 69 vesicles, 3 experiments.
See also Figure S1.

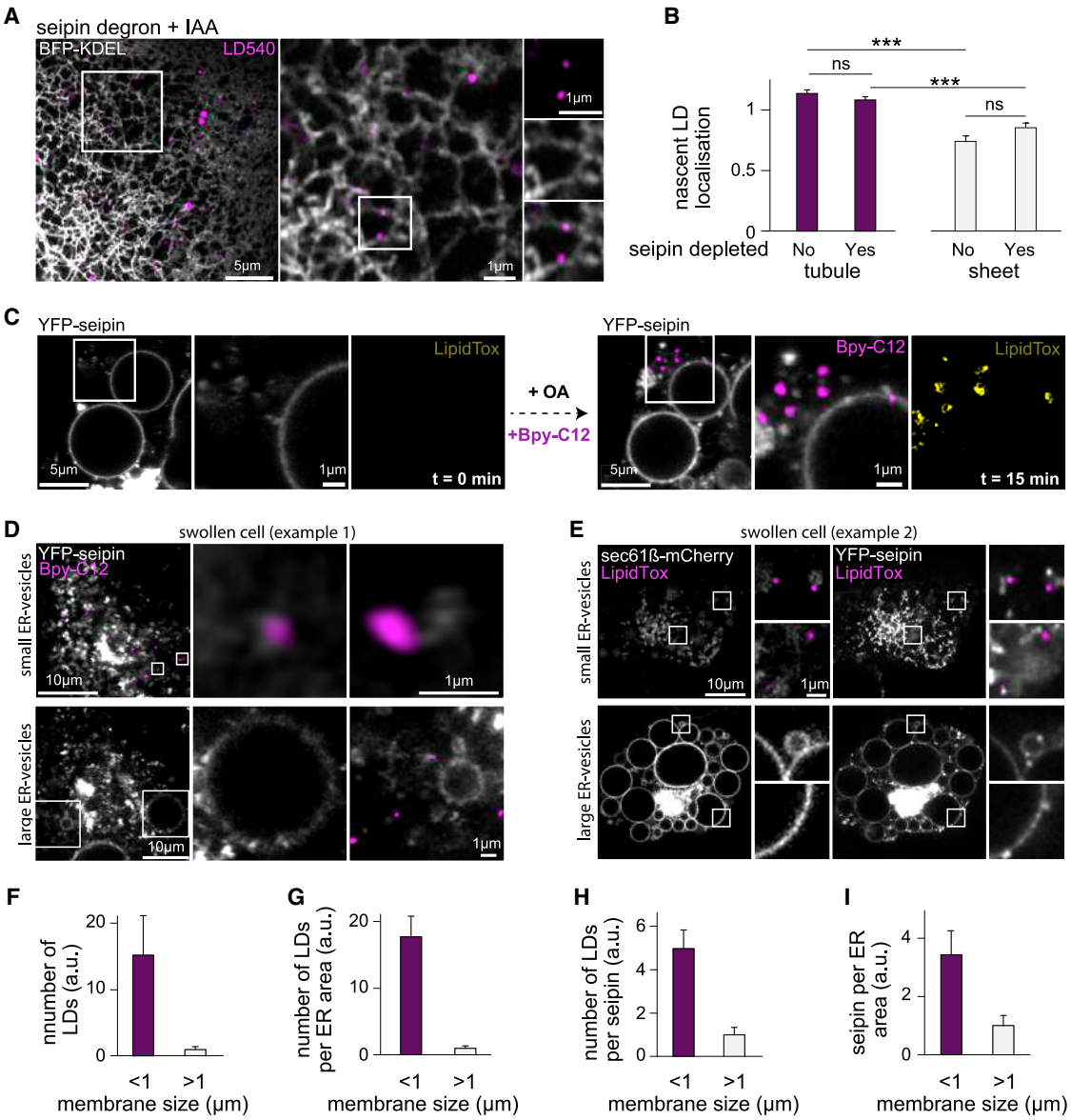

Figure 2. LDs Nucleate at ER Tubules in the Absence of Seipin and Not at Large Vesicles in the Presence of Seipin

(A) Seipin degron cells were treated and imaged as in Figure 1D. Seipin was depleted by adding IAA to the cells 18 h prior to imaging.

(B) Analysis of (A). The distribution of segmented ER pixels at nascent LDs was compared to overall pixel distribution of sheets/tubules in the same cells. Bars: mean ± SEM, n = 44–47 ROIs from 44–47 cells, 2 experiments (>1,000 LDs/group).

(C) Swollen Cos7 cells were imaged before and after OA and Bpy-C_{12} addition. Note Bpy-C_{12} and LipidTox colocalization in LDs.

(D) ER vesicles were induced in Cos7 cells expressing YFP-seipin and sec61β-mCherry and imaged 15 min after OA addition. Note submicrometric ER vesicles apposed to LDs.

(E) ER vesicles were induced in Cos7 cells expressing YFP-seipin and sec61β-mCherry and imaged 15 min after OA addition.

(F) Analysis of (D) and (E). LD number per ER vesicle size in swollen cells overexpressing seipin is shown. Mean ± SEM; n = 1,230 LDs, 4 experiments.

(G) Analysis of (D) and (E). LD number per ER vesicle size in (F) is normalized to sec61β signal, defined as the number of LDs per ER area. Mean ± SEM.

(H) Analysis of (D) and (E). Number of LDs normalized to seipin signal per ER vesicle size is shown, defined as the number of LDs per seipin signal. Mean ± SEM.

(I) Analysis of (D) and (E). Seipin intensity per ER vesicle is shown, normalized to sec61β signal, defined as seipin signal per ER area. Mean ± SEM.

See also Figure S2.

system. We used Cos7 cells transfected with mouse YFP-seipin, which were able to make LDs (Figure S2C). We next induced the formation of ER vesicles and added the NL dye LipidTox. We then fed the cells with OA and red Bodipy-C_{12} (Bpy-C_{12}) (1,000:1), previously shown to be incorporated into NLs [26, 38]. Accordingly, Bpy-C_{12} became incorporated into new LipidTox-positive LDs (Figures 2C and S2D), indicating that the swollen cells were capable of *de novo* LD formation, albeit slightly less efficiently than normal cells (Figure S2E). Interestingly, almost all generated Bpy-C_{12}-positive LDs appeared

near submicrometric seipin-positive vesicles (Figures 2C and 2D). We next performed similar experiments, transfecting the cells with YFP-seipin and sec61β-mCherry (to mark the ER), and fed the cells with OA, using LipidTox to label the formed LDs. Upon this treatment, the majority of forming LDs were also found on submicrometric ER vesicles (Figures 2E–2G and S2F) or in tubules co-existing with large ER vesicles (Figure S2G). The density of formed LDs per seipin signal was about 4 to 5 times higher at smaller ER vesicles than at larger ones (Figure 2H). Indeed, LDs rarely appeared at larger ER vesicles (Figures 2C–2G, S2F, and S2G), even though they contained clear seipin signal (Figures 1I, 2C–2E, 2I, S2F, and S2G). Thus, curvature per se and/or proteins localized to ER tubules facilitate LD assembly in both the absence and presence of seipin.

We previously reported that relocalization of seipin to the nuclear envelope (NE) was sufficient to relocate LD biogenesis to this site [28]. As the NE is a relatively flat membrane, this seemed at odds with our above observations suggesting that membrane curvature facilitates LD assembly. However, the GFP-nanobody-based confinement will trap seipin to both the NE as well as nearby ER tubules, and distinguishing between these two possibilities is not possible at the light microscopy resolution (Figure S2H). To investigate this further, we transfected cells with seipin trapped at the NE with the ER-LD marker peptide HPos and imaged LD formation in live cells. Interestingly, we found that, also in this situation, virtually all LDs formed in close proximity to nearby ER tubular structures (Figures S2I and S2J). Thus, LDs forming in the seipin NE-trapped cells may initially form at ER tubules in close proximity to the NE.

In summary, LDs preferentially form at ER tubules independently of seipin or the abundance of sheets. Because there is so far no protein known whose sole inhibition aborts LD formation, we hypothesize that membrane curvature is likely sufficient and mandatory to efficiently trigger LD assembly.

TGs Are Diffusive in ER Membranes, and Their Distribution and Assembly in LDs Are Curvature Dependent

Because LDs were mainly appearing from submicrometric ER vesicles, we thought that maybe larger vesicles were not capable of making NLs. To test this, we generated large ER vesicles in Cos7 cells and added LipidTox. We then fed the cells with OA to drive NL production. We found an increase in LipidTox signal in the large ER vesicles (Figures 3A and 3B), suggesting accumulation of NLs in the membrane. Indeed, in model membranes, increasing the concentration of TG increased LipidTox signal (Figure S3A). These data suggest that the large ER vesicles are able to synthesize NLs.

We next used Bpy-C_{12} to better monitor the distribution of NLs in ER vesicles. Similarly to red Bpy-C_{12}, also green Bpy-C_{12} was incorporated into newly formed LDs upon OA administration, in both WT and swollen cells (Figures S3B and S3C). In addition, a uniform Bpy-C_{12} signal was observed in ER vesicles (Figures 3C, 3D, and S3D). Similarly to LipidTox, the Bpy-C_{12} signal also increased over time, likely due to ongoing lipogenesis. This uniform Bpy-C_{12} signal rapidly recovered following photobleaching of a fraction of the membrane (Figure 3E), suggesting that the generated fluorescent NLs was freely diffusive in the membrane of the vesicle. Although Bpy-C_{12} is also known to be incorporated into PLs [26], the majority of the Bpy-C_{12} signal at ER vesicles under these conditions likely stems from NLs, as the fluorescence intensity of Bpy-C_{12} was much lower in the plasma membrane (a PL bilayer devoid of NLs) than at the ER (a PL bilayer harboring NLs; Figures S3E–S3I).

We next focused on the NL level relative to ER vesicle size. The concentration of Bpy-C_{12} signal was much higher in larger ER vesicles compared to smaller ones, as measured by comparing Bpy-C_{12} to sec61-mCherry signal (Figures 3F and 3G). Large vesicles were thus not defective in NL synthesis as compared to smaller ones and instead appeared to harbor more NLs. However, as found in Figure 2, we again observed that most LDs formed at smaller, submicrometric ER vesicles with lower Bpy-C_{12} membrane signal, rather than at the larger ER vesicles with higher Bpy-C_{12} signal (Figures 3H, 3I, and S3J). In line with this observation, HPos-positive LDs were also found on smaller vesicles (Figure S3K). These results suggest that, despite a lower concentration of NL in the membrane, smaller ER vesicles were more prone to support LD generation. This implies that the critical concentration of NLs to nucleate LDs may be lower on curved membranes compared to flat ones.

In agreement with our above conclusion, the depletion of seipin and Pex30 in yeast leads to large onion-ring-like ER membrane structures, low in curvature but full of NLs [39]. Analogously, our osmotic swelling treatment produced some cells with very-similar-appearing structures, rich in NLs but incapable of forming LDs (Figure 3J), despite the fact that all ER proteins are *a priori* present in these membranes. In comparison, in cells where submicrometric ER membranes were generated, LDs could be formed (Figure 3K).

Altogether, our data support the model that NLs synthesized in the ER membrane are initially freely diffusive. At a critical concentration, they condense into nascent LDs, phase separating from the bilayer. Our results suggest that flat membranes can accommodate a higher amount of NLs than curved membranes, implying that the critical concentration for nucleating LDs in flat areas is higher. By sufficiently diminishing this critical NL concentration, membrane curvature assists seipin to locally decrease the energy barrier and control LD nucleation.

The Presence of TG, but Not SE, Is Unfavorable in Tubules

Our hypothesis required proof that membrane curvature can modulate the distribution of TG molecules. We thus decided to study how NL distribution is altered by membrane curvature in a protein-free system. We employed the droplet-embedded vesicle system (DEV), composed of an artificial LD (aLD) embedded in a giant unilamellar vesicle (GUV) [40]. We made TG aLDs containing 0.5% of TG-NBD to report for TG localization. The GUVs were made of dioleoylphosphatidylcholine containing 0.5% rhodamine-DOPE (Rh-PE) to mark membranes and 0.5% of biotinylated PLs, enabling us to pull out tubules. When DEVs were made under these conditions, the aLD was in equilibrium with free TG molecules in the bilayer (Figure 4A), similarly as seen in the ER vesicles in Figure 3F. By using beads grafted with streptavidin and thereby binding biotinylated PLs, we pulled out tubules from the DEV and varied their radius by modulating the bilayer surface tension [41] (Figure 4B).

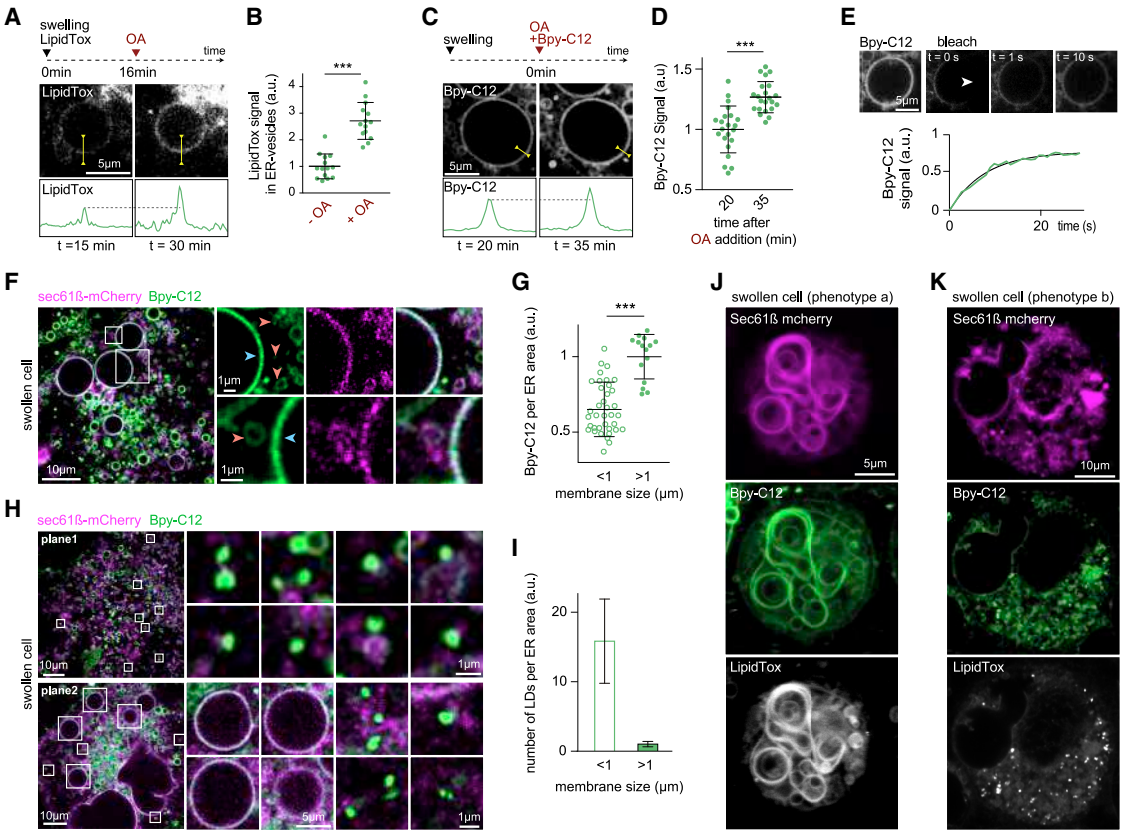

Figure 3. Neutral Lipid and LD Distribution in ER Vesicles

(A) ER vesicles were induced in Cos7 cells in the presence of LipidTox, and OA is added 16 min later. The LipidTox signal in an ER vesicle before and 15 min after OA addition is shown, with the membrane intensity profile displayed below the images.

(B) Analysis of (A). Mean ± SEM; n = 14 vesicles, 4 cells, 2 experiments.

(C) Bpy-C_{12} signal in Cos7 cell ER vesicles 20 min and 35 min after OA addition. Line scan shows an increase in signal.

(D) Analysis of (B). Mean ± SEM; n = 22 vesicles, 5 cells, 2 experiments.

(E) Rapid Bpy-C_{12} signal recovery in a partly bleached large ER vesicle; arrowhead indicates the bleached area. The recovery signal was normalized to that of non-bleached regions.

(F) ER vesicles induced in Cos7 cells expressing sec61β-mCherry were imaged 15 min after OA and Bpy-C_{12} addition. Bpy-C_{12} signal intensity is higher in large micrometric-sized vesicles (blue arrowhead) than in submicrometric vesicles (red arrowhead).

(G) Analysis of (F); mean ± SEM; n = 15–38 vesicles, 3 cells, 2 experiments.

(H) ER vesicles induced in Cos7 cells expressing sec61β-mCherry were imaged 15 min after OA and Bpy-C_{12} addition. Two planes of a single cell are shown. Most forming LDs are localized on submicrometric membranes.

(I) Analysis of (H). Number of LDs per ER vesicle size is shown. Mean ± SEM; n = 3,268 LDs, 4 experiments.

(J) A swollen Cos7 cell, expressing sec61β-mCherry and imaged 30 min after OA and Bpy-C_{12} addition, exhibits large onion-ring-like ER membrane structures full of NLs.

(K) Example of another cell treated as in (J), which has formed submicrometric ER structures and was able to assemble LDs.

See also Figure S3.

When the radius of the tube was decreased, we observed a clear reduction in the TG/PL ratio (Figure 4C). In other words, TG was more avidly excluded from the tubule to the flat membrane in comparison to PLs as curvature was increased (Figures 4D, 4E, and S4A). To rule out artifacts induced by TG-NBD, we performed analogous experiments without TG-NBD, using Bodipy dye to label membrane hydrophobicity. The signal evolution of Bodipy with regards to curvature was similar to that of TG-NBD (Figures S4B and S4C). These data indicate that it is unfavorable for highly curved membranes to bear free TG molecules. Here, because the tubule is in equilibrium with a flat region, the TG molecules simply escape from tubules to the flat region, where they seem to be of lower chemical potential, i.e., lower free energy per TG molecule. These findings are consistent with the TG distribution we previously found in ER vesicles (Figures 3F, 3G, and 3J).

We next compared the behavior of TG versus SE in this system. We used a TG solution containing ~29.5% SE, the maximum solubility of SE in TG that we could attain at room temperature, and 0.5% SE-NBD (Figures 4F, 4G, S4D, and S4E). Surprisingly, upon reduction of the tube radius, we found that the SE molecules remained on tubules and were relatively more enriched than PLs (Figure 4G). This is opposite to the behavior of TG alone (Figure 4E). To visualize TG localization in

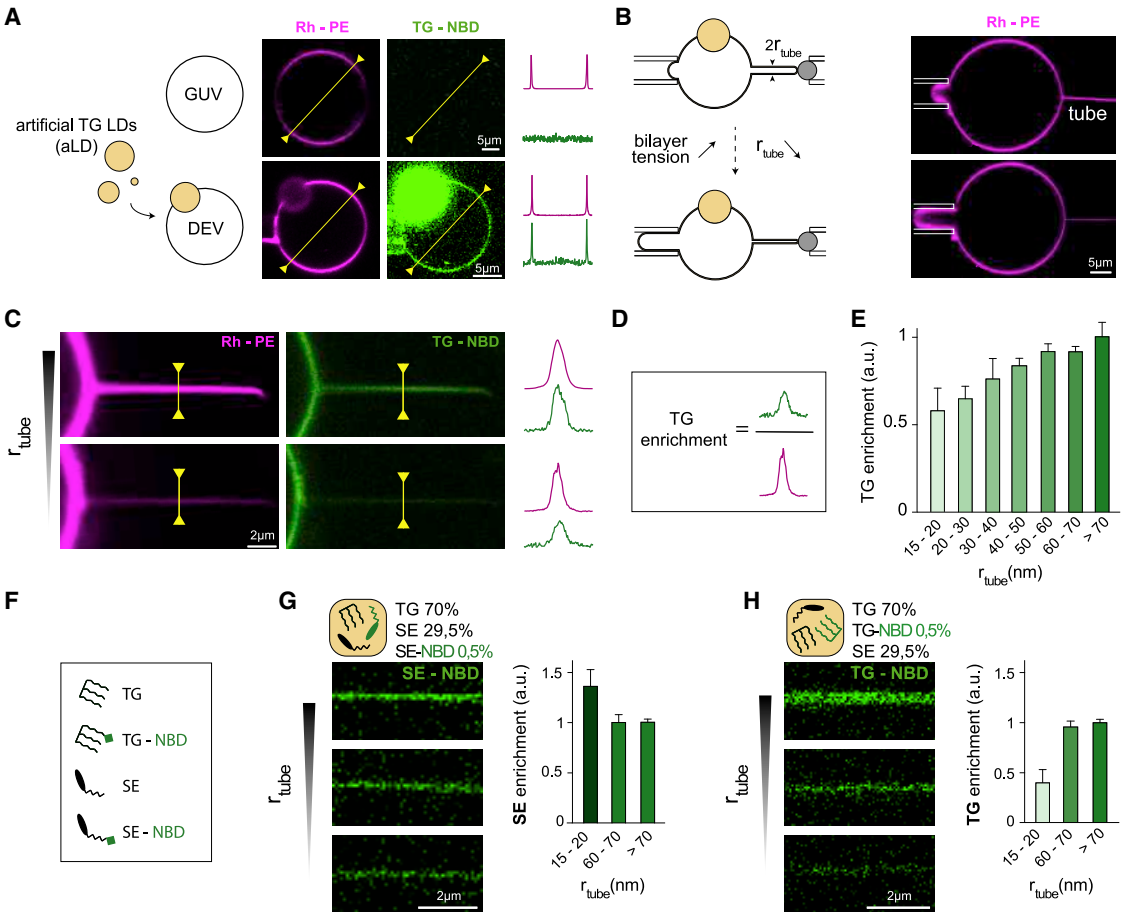

Figure 4. The Presence of TG, but Not SE, Is Unfavorable in Tubules

(A) Illustration of the DEV system consisting of GUVs mixed with aLDs. An exemplary DEV is shown. Rh-PE marks the membranes; TG-NBD marks the TG phase. The signal at the line scans (yellow lines) is shown.

(B) A nanotube is pulled from a DEV by using streptavidin-coated micro-beads bound to biotinylated PLs on the DEV. Increasing the bilayer tension with a micropipette decreases the tube radius.

(C) Nanotubes with 60-nm and 20-nm diameters are pulled from a DEV. Line scans on the tubes indicate that TG-NBD signal intensity is reduced relative to Rh-PE signal as the tube radius is decreased.

(D) Definition of the TG enrichment index in the tube.

(E) Analysis of (C). Plot of TG enrichment relative to the nanotube radius, r_{tube}, is shown. Mean ± SEM.

(F) Schematic description of different oil molecules used in (G) and (H). The green squares represent NBD.

(G) Nanotubes are pulled from DEVs as in (C), but the DEVs are made with aLDs containing TG, SE, and SE-NBD, as indicated (w/w). Analysis of the SE signal relative to tube radius is shown. Mean ± SEM.

(H) Same experiment as in (G) but with TG-NBD as indicated (w/w). Analysis of the TG signal relative to tube radius is shown. Mean ± SEM.

See also Figure S4.

this TG-SE mixture, we performed similar experiments but switching SE-NBD to TG-NBD (Figures 4F, 4H, and S4F). In this situation, we found that TG was still excluded from tubules (Figures 4H and S4F). These data revealed that membrane curvature demixed the TG-SE mixture: TG molecules were sorted out to flat regions although SE remained slightly enriched in tubules. Thus, TG and SE have different chemical potentials in tubules versus sheets.

The difference between TG and SE behavior in regards to membrane curvature was unexpected. To further study whether their dynamics were also differently altered, we simultaneously bleached both NBD and rhodamine signals, reporting for NLs and PLs, respectively. Photobleaching was performed on tubules (Figures 5A–5C) and at the flat apex region of the DEV (Figures S5A–S5C). On flat regions, we found that both TG and SE signals recovered faster than the PL signal, indicating that SE and TG were both more mobile than PLs (Figures 5D, S5B, and S5C). In contrast, in tubules, TG was slightly less mobile than PLs, although SE still remained faster (Figures 5B–5D). Thus, relative to PL motility, curvature slows down TG, but not SE.

Altogether, our above data revealed that the presence of independent TG molecules is unfavorable in curved regions. Furthermore, TG and SE have intrinsic static and dynamic behaviors discriminated by membrane curvature. They have different chemical potentials, energy per molecule, at flat and curved

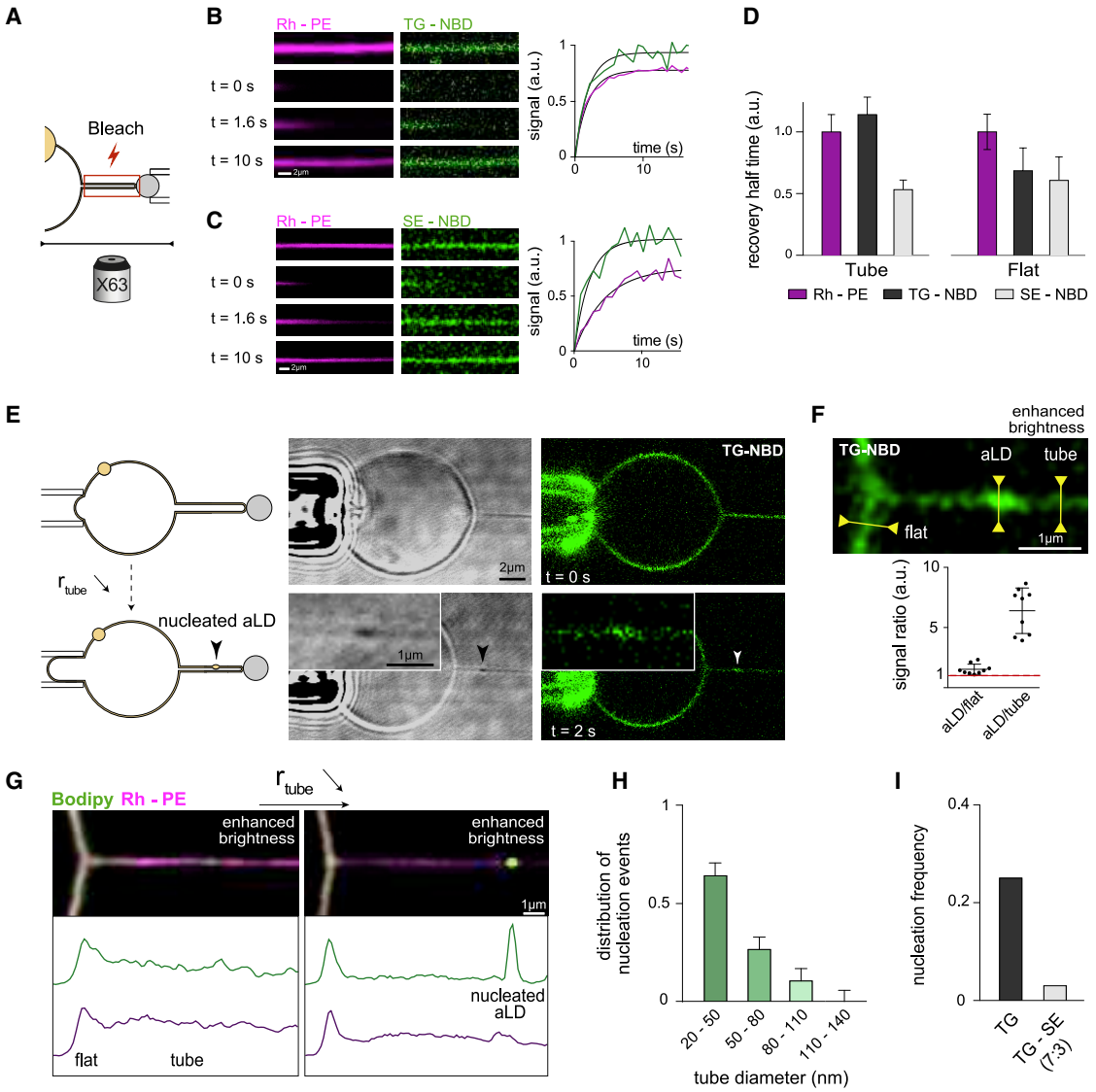

Figure 5. Membrane Curvature More Efficiently Triggers the Assembly of *In Vitro* TG Than SE LDs

(A) Diagram of the fluorescence recovery after photobleaching (FRAP) region where both Rh-PE and TG-NBD or SE-NBD are bleached in the entire nanotube.

(B) Representative time sequence of Rh-PE and TG-NBD recovery following photobleaching. The normalized fluorescence intensity evolution of the bleach region is shown with its fitting curve. Experiment was repeated three times.

(C) Representative time sequence of Rh-PE and SE-NBD recovery following photobleaching. The normalized fluorescence intensity evolution of the bleach region is shown with its fitting curve. Experiment was repeated three times.

(D) Analysis of (B) and (C). Plot of the average recovery half-time of Rh-PE, TG-NBD, and SE-NBD (normalized by Rh-PE) as a function of membrane curvature. Mean ± SEM. For examples of photobleaching recovery in flat membranes, see Figure S5.

(E) A nanotube is pulled from a DEV, and the bilayer was submitted to a sudden increase of surface tension to drastically increase tube curvature. An artificial TG LD is nucleated following this manipulation. The arrowhead shows the nucleated TG aLD shown in the inset.

(F) Smoothened image of the nucleated aLD from the inset in (E) is shown. For analysis of signal ratio, the intensity of the nucleated aLD signal is divided by the tube or the GUV intensity prior to nucleation. Bars: mean ± SEM, n = 9.

(G) An additional example of a nucleation event in a nanotube is shown with using TG only, labeled by Bodipy, which was added to the medium. Signal profiles along the tube of Rh-PE and Bodipy are shown before and after nucleation.

(H) Distribution of the nucleation events is reported against the final nanotube radius. Bars: mean ± measurement uncertainty, n = 9.

(I) Frequency of nucleation events observed relative to aLD NL composition. For TG, n = 9 nucleation events out of 36 trials; for TG-SE, n = 1 nucleation event out of 19 trials.

See also Figure S5.

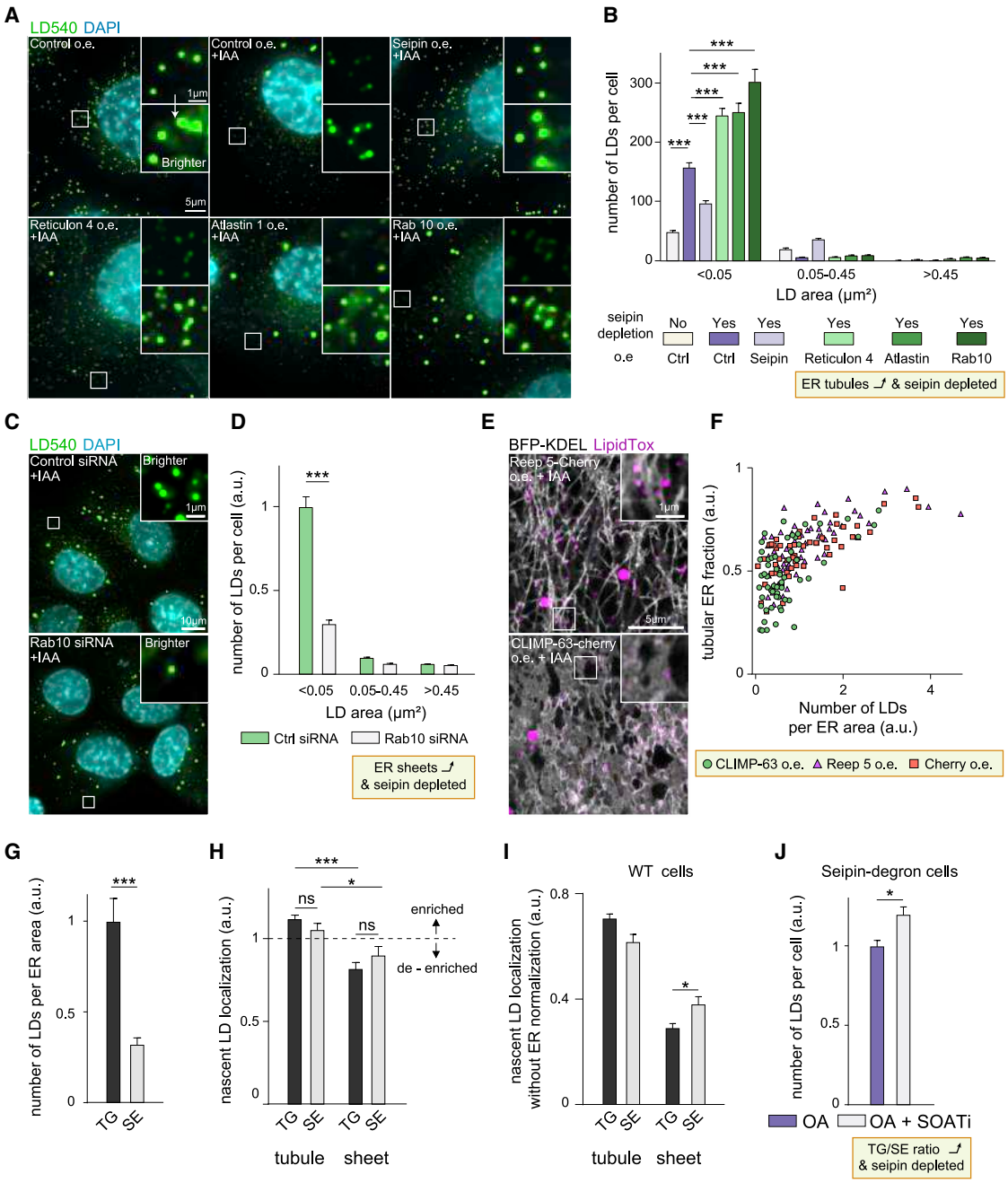

Figure 6. Modulation of Sheet/Tubule Ratio Alters LD Assembly

(A) ER tubule proteins were stably overexpressed in seipin degron cells. Cells were delipidated for 3 days, seipin was depleted by IAA treatment for 18 h, and LD biogenesis was induced by OA 1-h treatment. Cells were fixed, stained with LD540 and DAPI, and imaged by widefield microscopy. Maximum intensity projections of deconvolved z stacks are shown. The insets show tiny LDs; brightness is adjusted to display them more clearly.

(B) Analysis of (A). Bars: mean ± SEM, n = 167–549 cells/group, 2 experiments.

(C) Seipin degron cells were treated with control or Rab18 siRNA for 3 days in LPDS, including 18 h IAA treatment to deplete seipin. Cells were then treated with OA for 1 h, fixed, and stained as in (A). The insets show tiny LDs; brightness is adjusted to display them more clearly.

(D) Analysis of (C). Bars: mean ± SEM, n = 344–353 cells/group, 2 experiments.

(E) Seipin degron cells stably expressing BFP-KDEL were transfected with indicated plasmids for 2 days, including 1 day delipidation (LPDS and DGATi) and IAA treatment. After DGATi washout, cells were imaged live with Airyscan microscopy starting 45–75 min after OA addition in the presence of LipidTox Green.

(F) Analysis of (E). Peripheral ER ROIs were segmented for sheets and tubules using the BFP-KDEL channel and the number of LDs plotted (normalized to total ER area in each ROI) relative to ER morphology; n = 172 ROIs from 172 cells, 2 experiments.

(G–I) Cells were treated imaged and analyzed as in Figures 1D and 1E. Bars: mean ± SEM, n = 38–39 ROIs from 38–39 cells/group, 3 experiments (428–1,095 LD-associated seipins). The data for TG LDs are the same as in Figure 1E WT LDs. In (H), the distribution of segmented ER pixels at LD-associated seipin foci was

(legend continued on next page)

membrane areas. Thus, LD assembly mechanism likely depends on the NL composition.

Membrane Curvature Promotes TG LD Nucleation *In Vitro*

The presence of free TG molecules was more unfavorable in curved than flat regions (Figure 4E). Therefore, it could have been favorable for TG molecules to condense into droplets in tubules. However, TGs simply escaped from the tubule to the flat region, as they were part of a continuous system (Figure 4C). Under these static experimental conditions, there was no means by which to increase the concentration of TGs in tubules relative to PLs. In cells, ongoing lipogenesis guarantees that the concentration of TG in the ER membrane increases.

We reasoned that, if we rapidly decreased the tube radius faster than the NL diffusion time, we should be able to increase the local concentration of NL per PL in the tube. Starting from a tube diameter of around 200 nm, the radius was rapidly decreased by drastically increasing the DEV bilayer tension (Figure 5E). We observed nucleation events whereby TG molecules condensed in the tubule into lens-like or droplet shapes, as reported by TG-NBD or Bodipy signals (Figures 5E–5G and S5D–S5H). The TG signal in these droplets was greater than that observed in the flat or tubular bilayer regions prior to nucleation (Figures 5F, S5E, S5F, and S5I), supporting the notion that the TG molecules in the tubules had condensed. The success rate of nucleation increased with the decrease of the radius of the tubule (Figure 5H), either because the local concentration increased more or the effect of curvature was more pronounced. The nucleation of these model LDs was most often observed when the tube diameter was decreased to around 35 nm (Figure 5H), in the range of ER tubules [42].

Finally, as we had observed differences between TG and SE behavior in regards to membrane curvature, we repeated the previous experiment with a TG/SE (70/30) mixture. The success rate of nucleation in the presence of SE was much lower than that for TG alone (Figure 5I). These results suggest that membrane curvature more efficiently promotes the nucleation and assembly of TG- rather than SE-containing LDs. This divergence very likely pertains to the difference in chemical potential and mobility between the molecules (Figures 4G, 4H, and 5D). TG, which diffused more slowly and was unfavored at tubules, was more efficiently assembled into droplets as the curvature was increased.

These data suggest that membrane curvature can solely mediate LD nucleation, especially of TG droplets. This is due to the higher chemical potential of TG in tubular regions, which is annihilated by the spontaneous condensation of TG molecules into droplets.

Modulating ER Sheet-to-Tubule Ratio Alters LD Nucleation Frequency in Seipin-Deficient Cells

Two main conclusions can be derived from our *in vitro* approach (Figures 5H and 5I). First, curvature increases the chemical potential of TG and thereby catalyzes LD assembly. Second, the presence of SE has an inhibitory contribution on the curvature-induced LD assembly. If our model is correct, modulating ER tubule-to-sheet ratio could affect the number of assembled LDs during NL synthesis, and this could be altered by SE levels. Because seipin interferes with LD nucleation, its presence might mask the contribution of membrane curvature. We therefore decided to work on a reductionist cell system lacking seipin, wherein cells generate a large amount of tiny LDs that fail to grow [26, 27].

We first investigated the effect of increasing the amount of ER tubules. To this end, we stably transfected seipin degron cells with select ER-tubule-generating proteins: reticulon 4 [34]; atlastin 1 [43]; or Rab10 [44]. We then acutely removed seipin and induced LD generation by OA. Seipin removal led to the drastic increase of the tiny nucleated LDs, which could be efficiently rescued by the concomitant overexpression of seipin (Figures 6A and 6B). Overexpression of the tubule-generating proteins increased the number of LDs in this system (Figures 6A and 6B), suggesting that increasing tubules may enable higher number of LDs to be assembled.

We next studied the effect of increasing sheets at the expense of tubules. We previously observed that the number of *de novo* assembled LDs in seipin-depleted cells is markedly reduced by Rab18 KO [28], which increases ER sheets (Figure 1C). This observation supports the notion that increasing sheets at the expense of tubules decreases nucleation events. To further investigate this, we depleted Rab10 with small interfering RNAs (siRNAs) or treated the cells with the microtubule polymerizing drug nocodazole, both of which induce ER sheet expansion [44, 45]. These manipulations efficiently reduced the number of tiny nucleated LDs in seipin-depleted cells (Figures 6C, 6D, S6A, and S6B). In the presence of seipin, increasing ER sheets only mildly reduced the number of assembled LDs (Figures S6C and S6D).

To investigate this phenomenon in more detail, we modulated the ER tubule-to-sheet ratio in seipin-deficient cells and imaged them live during 45–75 min after OA administration. We modulated the sheet-to-tubule ratios by transient overexpression of mCherry-tagged ER shaping proteins CLIMP-63 (increasing sheets) or REEP-5 (increasing tubules) or soluble mCherry as control. We imaged peripheral ER regions with varying ER morphologies and found that regions of cells with higher ratios of tubules versus sheets typically had more LDs (Figures 6E and 6F). Overall, these data suggest that the number of LDs generated in seipin-deficient cells is linked to the ER sheet-to-tubule ratio, with an increase in sheets lowering the number of LDs.

Our *in vitro* data suggested that SEs have an inhibitory contribution to tubule-induced LD nucleation (Figure 5I). To test this hypothesis, we treated stringently starved cells with either 200 μM OA in the presence of SOAT1 inhibitor, to induce TG-enriched LDs, or 200 μM cholesterol-cyclodextrin in the presence of DGAT1 and DGAT2 inhibitors, to induce SE-enriched LDs,

compared to the overall pixel distribution of sheets/tubules in the same cells; in (I), the distribution of segmented ER pixels at LD-associated seipin foci is shown without normalization to overall ER pixel distribution.

(J) Seipin degron cells were delipidated for 3 days (including 18 h with DGATi) and treated with OA with or without SOAT inhibitor for 1 h, fixed, stained, and analyzed for LD sizes as in (A). Bars: mean ± SEM, n = 308–368 cells/group, 2 experiments.

See also Figure S6.

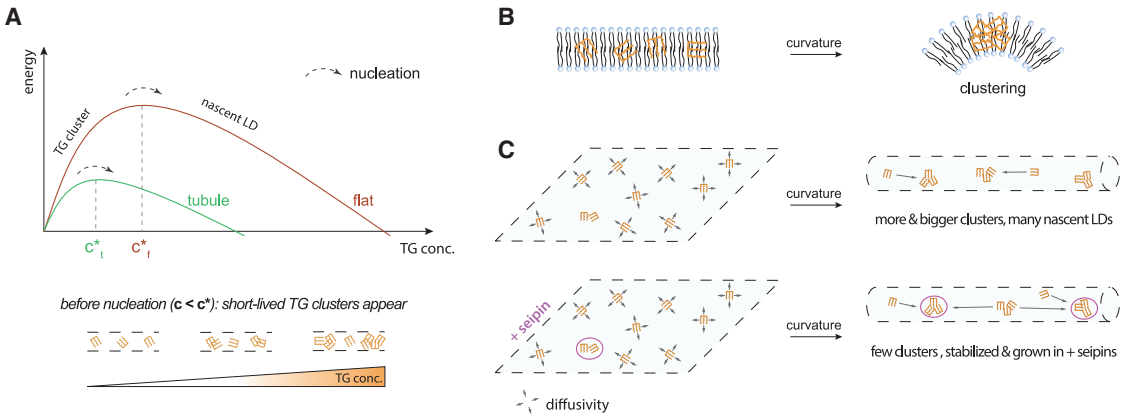

Figure 7. Model for the Role of Curvature and Seipin in Triggering LD Assembly

(A) Top panel: illustration of the energy profile of phase transitions in the context of LD assembly. Curvature decreases the critical concentration and the energy barrier for nucleation. Bottom panel: before the critical nucleation concentration, c*, short-lived TG clusters appear (ms). Above this concentration, nascent droplets form.

(B) Proposed mechanism by which curvature favors TG clustering by exposing the hydrophobic core to water molecules.

(C) Without seipin, many TG clusters are triggered at tubules and transit into nascent droplets (bottom). Seipin stabilizes clusters in tubules, and TGs favorably move to these seipin-stabilized clusters, which will turn into nascent LDs, fewer in number than without seipin.

and imaged live nascent LDs. Despite equimolar lipid loading, OA induced a much higher number of LDs compared to cholesterol (Figures 6G and S6E), which agrees with our prediction, although we cannot rule out differences in efficiencies of the enzymes involved. Nascent SE-LDs were also more prevalent at ER tubules than sheets, albeit with a slight preference for sheets in comparison with TG-LDs (Figures 6H and 6I). Finally, the number of LD assembly events in seipin-depleted cells could be increased by a concomitant treatment of cells with OA and SOAT1 inhibitor, i.e., by increasing the TG/SE ratio (Figure 6J). These observations are well in line with our *in vitro* data that TG LDs are more efficiently assembled than SE LDs and that SE has an inhibitory effect on LD nucleation.

Altogether, these data suggest that the number of TG LD assembly events is determined by the abundance of ER tubules in the absence of seipin and that seipin controls the number of LD assembly sites.

DISCUSSION

Here, we studied the initial step of LD assembly, nucleation, which is the condensation of freely diffusing NL molecules. This process occurs when an energy barrier is crossed (Figure 7A), and this barrier is associated with a critical concentration of NLs [7]. Our findings suggest that membrane curvature decreases this energy barrier and the associated critical concentration (Figure 7A). This happens because curvature particularly increases the chemical potential of a TG molecule. In this thermodynamic scenario, this increase of potential reduces the energy gap to the nucleation barrier. By doing so, membrane curvature catalyzes LD nucleation at tubules (Figure 7A).

The molecular mechanism by which membrane curvature increases the chemical potential of TG is unknown. Nonetheless, one of the major effects of curvature on membranes is to space PLs and to expose their hydrophobic core to water (Figure 7B). Thus, TG molecules might be more exposed to water molecules in a bilayer with higher curvature. To minimize this contact, TGs can escape from highly curved regions by diffusing to less curved ones or by clustering and condensing into droplets (Figures 7A and 7B). Indeed, the latter situation minimizes the total free energy, similarly as when oil droplets merge to minimize the total oil/water contact area.

There may be several reasons for the unexpected difference between TG and SE behavior in regards to membrane curvature. The difference in TG and SE chemistry should lead to *a priori* different interaction profiles with molecules in their environment, impacting their tendency to condense in membranes. In addition, these NLs may adopt different conformations in tubules. One could imagine the possibility that SE remains parallel to PLs although TG would be perpendicular to them or vice versa. Such organization would influence their contact with water molecules and with PLs and hence their propensity to condense.

The thermodynamic framework underlining phase separation is well documented, and we have previously described it in the context of LD assembly [7]. It predicts that, before the critical concentration for nucleation is reached, TG clusters appear and resorb rapidly, at a frequency increasing with the concentration of free TG (Figure 7A). The formation of such clusters would slow down TG diffusion, in line with our results indicating that membrane curvature reduces TG diffusion (Figures 5B and 5D). When the TG concentration reaches a critical nucleation concentration, larger clusters will transit into nascent LDs or lenses (Figure 7A). On flat membranes, this critical concentration is estimated to be 3%–5% of TG to PLs [6, 12]. On curved membranes, this value is expected to be smaller (Figure 7A). Consequently, membrane curvature should increase the frequency of appearance of unstable TG clusters and hence the likelihood that they transit into stable, nascent LDs (Figure 7C). Such a spontaneous process would lead to uncontrolled LD assembly, sporadically triggered at and by tubules.

Because seipin can dictate where LDs form [28] and seipin controls the number of LD assembly events on tubules (this

study), it has to act very early to aid some clusters to jump the energy hill and transit into nascent LDs (Figures 7A and 7C). Indeed, recent results show that the seipin/promethin complex forms a LD assembly complex copurifying with TG molecules [46]. Our data support that seipin would foster some TG clusters and controls their transition into stable, nascent LDs (Figure 7C). Concretely, seipin might diffuse and detect TG clusters in tubules and/or the clusters might directly appear at seipin oligomers, because favorable protein-lipid interactions can trigger phase separation [7]. In any case, by controlling the transition of some TG clusters into nascent LDs, seipin guarantees that only seipin-positive TG clusters get stabilized and grow. As these nascent LDs grow, the local concentration of TG in the tubule decreases, inhibiting LD assembly close to seipin-defined sites [28]. In the absence of seipin, LD assembly is more dominated by curvature and many more TG clusters will transit into nascent LDs, controlled by the abundance of ER tubules (Figures 6 and 7C).

Interestingly, seipin-collaborating proteins, from plant to human cells, seem to be membrane curvature sensors or inducers. These include the membrane-shaping protein PEX30/MCTP2 [31, 39], promethin, Ldo16/45 [47, 48], and LDIP [49]. The induction of local curvature by these proteins could facilitate nucleation and trigger LD assembly at specific sites determined by seipin. Indeed, the concomitant depletion of Pex30 and seipin did not alter TG synthesis but rather their packaging into LDs, with TG molecules remaining in large onion-like multilamellar ER vesicles [39], similarly as observed in Figure 3J. These structures are of almost zero curvature and are unable to make LDs. LDs did not efficiently form on large ER vesicles (Figures 2 and 3) that contained abundant levels of seipin, suggesting that seipin activity in LD assembly relies on membrane curvature (Figure 7C).

In conclusion, we unveiled how NLs are distributed in membranes and found that membrane curvature catalyzes their assembly into LDs, in cooperation with seipin. Our results shed light on the role of ER topology on LD biogenesis and pave the way for further studies addressing how curvature is coupled to the function of seipin and other proteins regulating LD biogenesis.

STAR★METHODS

Detailed methods are provided in the online version of this paper and include the following:

- KEY RESOURCES TABLE
- RESOURCE AVAILABILITY
  - Lead Contact
  - Materials Availability
  - Data and Code Availability
- EXPERIMENTAL MODEL AND SUBJECT DETAILS
  - Mammalian cells
- METHOD DETAILS
  - siRNAs and plasmids
  - Stable cell lines
  - Large ER-derived Intra-Cellular vesicle experiments
  - Delipidation, DGATi Treatments, LD Induction, seipin depletion with IAA, SNAP-labeling
  - Live cell analysis of LD formation sites and ER morphology
  - LD analysis of fixed cells
  - DEV preparation
  - Micromanipulation
  - Nanotube formation and radius modulation by micro aspiration
  - Nanotube radius measurements with fluorescence calibration
  - Surface tension measurements
  - Tube modulation and TG distribution experiments
  - FRAP experiments
- QUANTIFICATION AND STATISTICAL ANALYSIS
  - Image analysis of swelling experiments and *in vitro* studies
  - Statistical analysis

SUPPLEMENTAL INFORMATION

Supplemental Information can be found online at https://doi.org/10.1016/j.cub.2020.04.066.

ACKNOWLEDGMENTS

We thank Anna Uro and Katharina Ven for excellent technical assistance and the Thiam team members and Dr. Lionel Fôret for their critical discussions and advice. This study was supported by the Academy of Finland (grants 282192, 312491, and 307415 to E.I.), Sigrid Juselius Foundation (E.I.), and ANR-17-CE11-0003-NANODROP and ANR-18-CE11-0012-01-MOBIL to A.R.T. We thank Biocenter Finland and HiLIFE light microscopy and flow cytometry units. V.T.S. acknowledges support from the Finnish Medical, Paulo, Alfred Kordelin, Maud Kuistila, Biomedicum Helsinki, and Emil Aaltonen Foundation. A.S. is supported by Q-life program. We apologize to our colleagues whose works could not be cited due to space restrictions.

AUTHOR CONTRIBUTIONS

A.R.T., E.I., V.T.S., and A.S. designed experiments; A.S. performed *in vitro* and intra-cellular vesicle experiments, with the help of M.O. and A.C.; V.T.S. performed experiments in A431 cells with the help of S.L. and X.Z.; and A.R.T., E.I., V.T.S., and A.S. analyzed data and wrote the manuscript.

DECLARATION OF INTERESTS

The authors declare no competing interests.

Received: December 12, 2019
Revised: March 24, 2020
Accepted: April 23, 2020
Published: May 21, 2020

REFERENCES

1. Olzmann, J.A., and Carvalho, P. (2019). Dynamics and functions of lipid droplets. Nat. Rev. Mol. Cell Biol. *20*, 137–155.
2. Gao, M., Huang, X., Song, B.-L., and Yang, H. (2019). The biogenesis of lipid droplets: lipids take center stage. Prog. Lipid Res. *75*, 100989.
3. Walther, T.C., Chung, J., and Farese, R.V., Jr. (2017). Lipid droplet biogenesis. Annu. Rev. Cell Dev. Biol. *33*, 491–510.
4. Choudhary, V., Ojha, N., Golden, A., and Prinz, W.A. (2015). A conserved family of proteins facilitates nascent lipid droplet budding from the ER. J. Cell Biol. *211*, 261–271.

5. Ben M'barek, K., Ajjaji, D., Chorlay, A., Vanni, S., Forêt, L., and Thiam, A.R. (2017). ER membrane phospholipids and surface tension control cellular lipid droplet formation. Dev. Cell *41*, 591–604.e7.

6. Khandelia, H., Duelund, L., Pakkanen, K.I., and Ipsen, J.H. (2010). Triglyceride blisters in lipid bilayers: implications for lipid droplet biogenesis and the mobile lipid signal in cancer cell membranes. PLoS ONE *5*, e12811.

7. Thiam, A.R., and Forêt, L. (2016). The physics of lipid droplet nucleation, growth and budding. Biochim. Biophys. Acta *1861* (8 Pt A), 715–722.

8. Salo, V.T., and Ikonen, E. (2019). Moving out but keeping in touch: contacts between endoplasmic reticulum and lipid droplets. Curr. Opin. Cell Biol. *57*, 64–70.

9. Chorlay, A., Monticelli, L., Veríssimo Ferreira, J., Ben M'barek, K., Ajjaji, D., Wang, S., Johnson, E., Beck, R., Omrane, M., Beller, M., et al. (2019). Membrane asymmetry imposes directionality on lipid droplet emergence from the ER. Dev. Cell *50*, 25–42.e7.

10. Choudhary, V., Golani, G., Joshi, A.S., Cottier, S., Schneiter, R., Prinz, W.A., and Kozlov, M.M. (2018). Architecture of lipid droplets in endoplasmic reticulum is determined by phospholipid intrinsic curvature. Curr. Biol. *28*, 915–926.e9.

11. Zanghellini, J., Wodlei, F., and von Grünberg, H.H. (2010). Phospholipid demixing and the birth of a lipid droplet. J. Theor. Biol. *264*, 952–961.

12. Hamilton, J.A., Miller, K.W., and Small, D.M. (1983). Solubilization of triolein and cholesteryl oleate in egg phosphatidylcholine vesicles. J. Biol. Chem. *258*, 12821–12826.

13. Puhka, M., Vihinen, H., Joensuu, M., and Jokitalo, E. (2007). Endoplasmic reticulum remains continuous and undergoes sheet-to-tubule transformation during cell division in mammalian cells. J. Cell Biol. *179*, 895–909.

14. Hariri, H., Rogers, S., Ugrankar, R., Liu, Y.L., Feathers, J.R., and Henne, W.M. (2018). Lipid droplet biogenesis is spatially coordinated at ER-vacuole contacts under nutritional stress. EMBO Rep. *19*, 57–72.

15. Hsieh, K., Lee, Y.K., Londos, C., Raaka, B.M., Dalen, K.T., and Kimmel, A.R. (2012). Perilipin family members preferentially sequester to either triacylglycerol-specific or cholesteryl-ester-specific intracellular lipid storage droplets. J. Cell Sci. *125*, 4067–4076.

16. Meyers, A., Del Rio, Z.P., Beaver, R.A., Morris, R.M., Weiskittel, T.M., Alshibli, A.K., Mannik, J., Morrell-Falvey, J., and Dalhaimer, P. (2016). Lipid droplets form from distinct regions of the cell in the fission yeast Schizosaccharomyces pombe. Traffic *17*, 657–669.

17. Nettebrock, N.T., and Bohnert, M. (2020). Born this way–biogenesis of lipid droplets from specialized ER subdomains. Biochim. Biophys. Acta Mol. Cell Biol. Lipids *1865*, 158448.

18. Fei, W., Shui, G., Gaeta, B., Du, X., Kuerschner, L., Li, P., Brown, A.J., Wenk, M.R., Parton, R.G., and Yang, H. (2008). Fld1p, a functional homologue of human seipin, regulates the size of lipid droplets in yeast. J. Cell Biol. *180*, 473–482.

19. Szymanski, K.M., Binns, D., Bartz, R., Grishin, N.V., Li, W.-P., Agarwal, A.K., Garg, A., Anderson, R.G., and Goodman, J.M. (2007). The lipodystrophy protein seipin is found at endoplasmic reticulum lipid droplet junctions and is important for droplet morphology. Proc. Natl. Acad. Sci. USA *104*, 20890–20895.

20. Binns, D., Lee, S., Hilton, C.L., Jiang, Q.-X., and Goodman, J.M. (2010). Seipin is a discrete homooligomer. Biochemistry *49*, 10747–10755.

21. Sui, X., Arlt, H., Brock, K.P., Lai, Z.W., DiMaio, F., Marks, D.S., Liao, M., Farese, R.V., Jr., and Walther, T.C. (2018). Cryo-electron microscopy structure of the lipid droplet-formation protein seipin. J. Cell Biol. *217*, 4080–4091.

22. Yan, R., Qian, H., Lukmantara, I., Gao, M., Du, X., Yan, N., and Yang, H. (2018). Human SEIPIN binds anionic phospholipids. Dev. Cell *47*, 248–256.e4.

23. Magré, J., Delépine, M., Khallouf, E., Gedde-Dahl, T., Jr., Van Maldergem, L., Sobel, E., Papp, J., Meier, M., Mégarbané, A., Bachy, A., et al.; BSCL Working Group (2001). Identification of the gene altered in Berardinelli-Seip congenital lipodystrophy on chromosome 11q13. Nat. Genet. *28*, 365–370.

24. Guillén-Navarro, E., Sánchez-Iglesias, S., Domingo-Jiménez, R., Victoria, B., Ruiz-Riquelme, A., Rábano, A., Loidi, L., Beiras, A., González-Méndez, B., Ramos, A., et al. (2013). A new seipin-associated neurodegenerative syndrome. J. Med. Genet. *50*, 401–409.

25. Windpassinger, C., Auer-Grumbach, M., Irobi, J., Patel, H., Petek, E., Hörl, G., Malli, R., Reed, J.A., Dierick, I., Verpoorten, N., et al. (2004). Heterozygous missense mutations in BSCL2 are associated with distal hereditary motor neuropathy and Silver syndrome. Nat. Genet. *36*, 271–276.

26. Salo, V.T., Belevich, I., Li, S., Karhinen, L., Vihinen, H., Vigouroux, C., Magré, J., Thiele, C., Hölttä-Vuori, M., Jokitalo, E., and Ikonen, E. (2016). Seipin regulates ER-lipid droplet contacts and cargo delivery. EMBO J. *35*, 2699–2716.

27. Wang, H., Becuwe, M., Housden, B.E., Chitraju, C., Porras, A.J., Graham, M.M., Liu, X.N., Thiam, A.R., Savage, D.B., Agarwal, A.K., et al. (2016). Seipin is required for converting nascent to mature lipid droplets. eLife *5*, e16582.

28. Salo, V.T., Li, S., Vihinen, H., Hölttä-Vuori, M., Szkalisity, A., Horvath, P., Belevich, I., Peränen, J., Thiele, C., Somerharju, P., et al. (2019). Seipin facilitates triglyceride flow to lipid droplet and counteracts droplet ripening via endoplasmic reticulum contact. Dev. Cell *50*, 478–493.e9.

29. Pagac, M., Cooper, D.E., Qi, Y., Lukmantara, I.E., Mak, H.Y., Wu, Z., Tian, Y., Liu, Z., Lei, M., Du, X., et al. (2016). SEIPIN regulates lipid droplet expansion and adipocyte development by modulating the activity of glycerol-3-phosphate acyltransferase. Cell Rep. *17*, 1546–1559.

30. Xu, D., Li, Y., Wu, L., Li, Y., Zhao, D., Yu, J., Huang, T., Ferguson, C., Parton, R.G., Yang, H., and Li, P. (2018). Rab18 promotes lipid droplet (LD) growth by tethering the ER to LDs through SNARE and NRZ interactions. J. Cell Biol. *217*, 975–995.

31. Joshi, A.S., Nebenfuehr, B., Choudhary, V., Satpute-Krishnan, P., Levine, T.P., Golden, A., and Prinz, W.A. (2018). Lipid droplet and peroxisome biogenesis occur at the same ER subdomains. Nat. Commun. *9*, 2940.

32. Kassan, A., Herms, A., Fernández-Vidal, A., Bosch, M., Schieber, N.L., Reddy, B.J., Fajardo, A., Gelabert-Baldrich, M., Tebar, F., Enrich, C., et al. (2013). Acyl-CoA synthetase 3 promotes lipid droplet biogenesis in ER microdomains. J. Cell Biol. *203*, 985–1001.

33. Shibata, Y., Shemesh, T., Prinz, W.A., Palazzo, A.F., Kozlov, M.M., and Rapoport, T.A. (2010). Mechanisms determining the morphology of the peripheral ER. Cell *143*, 774–788.

34. Voeltz, G.K., Prinz, W.A., Shibata, Y., Rist, J.M., and Rapoport, T.A. (2006). A class of membrane proteins shaping the tubular endoplasmic reticulum. Cell *124*, 573–586.

35. Gerondopoulos, A., Bastos, R.N., Yoshimura, S., Anderson, R., Carpanini, S., Aligianis, I., Handley, M.T., and Barr, F.A. (2014). Rab18 and a Rab18 GEF complex are required for normal ER structure. J. Cell Biol. *205*, 707–720.

36. Jaiswal, A., Hoerth, C.H., Zúñiga Pereira, A.M., and Lorenz, H. (2019). Improved spatial resolution by induced live cell and organelle swelling in hypotonic solutions. Sci. Rep. *9*, 12911.

37. King, C., Sengupta, P., Seo, A.Y., and Lippincott-Schwartz, J. (2020). ER membranes exhibit phase behavior at sites of organelle contact. Proc. Natl. Acad. Sci. USA *117*, 7225–7235.

38. Rambold, A.S., Cohen, S., and Lippincott-Schwartz, J. (2015). Fatty acid trafficking in starved cells: regulation by lipid droplet lipolysis, autophagy, and mitochondrial fusion dynamics. Dev. Cell *32*, 678–692.

39. Wang, S., Idrissi, F.-Z., Hermansson, M., Grippa, A., Ejsing, C.S., and Carvalho, P. (2018). Seipin and the membrane-shaping protein Pex30 cooperate in organelle budding from the endoplasmic reticulum. Nat. Commun. *9*, 2939.

40. Chorlay, A., and Thiam, A.R. (2018). An asymmetry in monolayer tension regulates lipid droplet budding direction. Biophys. J. *114*, 631–640.

41. Hochmuth, R.M., and Evans, E.A. (1982). Extensional flow of erythrocyte membrane from cell body to elastic tether. I. Analysis. Biophys. J. *39*, 71–81.

42. West, M., Zurek, N., Hoenger, A., and Voeltz, G.K. (2011). A 3D analysis of yeast ER structure reveals how ER domains are organized by membrane curvature. J. Cell Biol. *193*, 333–346.

43. Hu, J., Shibata, Y., Zhu, P.-P., Voss, C., Rismanchi, N., Prinz, W.A., Rapoport, T.A., and Blackstone, C. (2009). A class of dynamin-like GTPases involved in the generation of the tubular ER network. Cell *138*, 549–561.

44. English, A.R., and Voeltz, G.K. (2013). Rab10 GTPase regulates ER dynamics and morphology. Nat. Cell Biol. *15*, 169–178.

45. Joensuu, M., Belevich, I., Rämö, O., Nevzorov, I., Vihinen, H., Puhka, M., Witkos, T.M., Lowe, M., Vartiainen, M.K., and Jokitalo, E. (2014). ER sheet persistence is coupled to myosin 1c-regulated dynamic actin filament arrays. Mol. Biol. Cell *25*, 1111–1126.

46. Chung, J., Wu, X., Lambert, T.J., Lai, Z.W., Walther, T.C., and Farese, R.V., Jr. (2019). LDAF1 and seipin form a lipid droplet assembly complex. Dev. Cell *51*, 551–563.e7.

47. Eisenberg-Bord, M., Mari, M., Weill, U., Rosenfeld-Gur, E., Moldavski, O., Castro, I.G., Soni, K.G., Harpaz, N., Levine, T.P., Futerman, A.H., et al. (2018). Identification of seipin-linked factors that act as determinants of a lipid droplet subpopulation. J. Cell Biol. *217*, 269–282.

48. Teixeira, V., Johnsen, L., Martínez-Montañés, F., Grippa, A., Buxó, L., Idrissi, F.-Z., Ejsing, C.S., and Carvalho, P. (2018). Regulation of lipid droplets by metabolically controlled Ldo isoforms. J. Cell Biol. *217*, 127–138.

49. Pyc, M., Cai, Y., Gidda, S.K., Yurchenko, O., Park, S., Kretzschmar, F.K., Ischebeck, T., Valerius, O., Braus, G.H., Chapman, K.D., et al. (2017). Arabidopsis lipid droplet-associated protein (LDAP) - interacting protein (LDIP) influences lipid droplet size and neutral lipid homeostasis in both leaves and seeds. Plant J. *92*, 1182–1201.

50. Thiam, A.R., Antonny, B., Wang, J., Delacotte, J., Wilfling, F., Walther, T.C., Beck, R., Rothman, J.E., and Pincet, F. (2013). COPI buds 60-nm lipid droplets from reconstituted water-phospholipid-triacylglyceride interfaces, suggesting a tension clamp function. Proc. Natl. Acad. Sci. USA *110*, 13244–13249.

51. Spandl, J., White, D.J., Peychl, J., and Thiele, C. (2009). Live cell multicolor imaging of lipid droplets with a new dye, LD540. Traffic *10*, 1579–1584.

52. Goldstein, J.L., Basu, S.K., and Brown, M.S. (1983). Receptor-mediated endocytosis of low-density lipoprotein in cultured cells. Methods Enzymol. *98*, 241–260.

53. Elbashir, S.M., Harborth, J., Lendeckel, W., Yalcin, A., Weber, K., and Tuschl, T. (2001). Duplexes of 21-nucleotide RNAs mediate RNA interference in cultured mammalian cells. Nature *411*, 494–498.

54. Zurek, N., Sparks, L., and Voeltz, G. (2011). Reticulon short hairpin transmembrane domains are used to shape ER tubules. Traffic *12*, 28–41.

55. Friedman, J.R., Lackner, L.L., West, M., DiBenedetto, J.R., Nunnari, J., and Voeltz, G.K. (2011). ER tubules mark sites of mitochondrial division. Science *334*, 358–362.

56. Schindelin, J., Arganda-Carreras, I., Frise, E., Kaynig, V., Longair, M., Pietzsch, T., Preibisch, S., Rueden, C., Saalfeld, S., Schmid, B., et al. (2012). Fiji: an open-source platform for biological-image analysis. Nat. Methods *9*, 676–682.

57. Carpenter, A.E., Jones, T.R., Lamprecht, M.R., Clarke, C., Kang, I.H., Friman, O., Guertin, D.A., Chang, J.H., Lindquist, R.A., Moffat, J., et al. (2006). CellProfiler: image analysis software for identifying and quantifying cell phenotypes. Genome Biol. *7*, R100.

58. Berg, S., Kutra, D., Kroeger, T., Straehle, C.N., Kausler, B.X., Haubold, C., Schiegg, M., Ales, J., Beier, T., Rudy, M., et al. (2019). ilastik: interactive machine learning for (bio)image analysis. Nat. Methods *16*, 1226–1232.

59. Li, S., Prasanna, X., Salo, V.T., Vattulainen, I., and Ikonen, E. (2019). An efficient auxin-inducible degron system with low basal degradation in human cells. Nat. Methods *16*, 866–869.

60. Hölttä-Vuori, M., Salo, V.T., Ohsaki, Y., Suster, M.L., and Ikonen, E. (2013). Alleviation of seipinopathy-related ER stress by triglyceride storage. Hum. Mol. Genet. *22*, 1157–1166.

STAR★METHODS

KEY RESOURCES TABLE

REAGENT or RESOURCE	SOURCE	IDENTIFIER
Antibodies		
Mouse anti-Xpress (IF 1:500)	Thermo Fisher	R910-25; RRID: AB_2556552
Alexa 647 anti-mouse (IF 1:400)	Thermo Fisher	A-31571
Chemicals, Peptides, and Recombinant Proteins		
LD540 (fixed cells 0.1 μg/ml, live cells 0.03-0.05 μg/ml)	Princeton BioMolecular Research [51]	N/A
DAPI (10 μg/ml)	Sigma	D9542
Prolong Live Anti-Fade (1:100)	Thermo Fisher	P36975
Lipofectamine LTX and Plus Reagent	Thermo Fisher	15338100
Hiperfect	QIAGEN	301705
X-tremeGENE 9 DNA Transfection Reagent	Roche	N/A
Fetal bovine serum	Life Technologies	16000044
penicillin-streptomycin	Life Technologies	15140163
DGAT1 inhibitor (5 μM)	Sigma	PZ0207
DGAT2 inhibitor (5 μM)	Sigma	PZ0233
SOAT inhibitor (2 μg/ml)	Sigma	S9318
Indole-3-acetic acid sodium (500 μM)	Santa Cruz	Sc-215171
Cell-SIR647 (0.3 μM)	New England Biolabs	S9102S
Geneticin (G418) sulfate (0.6 mg/ml)	GIBCO	11811-031
Zeocin (0.2 mg/ml)	Invitrogen	R25001 GIBCO
Human fibronectin	Roche Diagnostics	11051407001 Roche
Formaldehyde	Sigma	P-6148
Nocodazole (20 μM)	Sigma	M1404
Cholesterol	Sigma	C8667
Methyl-β-cyclodextrin	Sigma	C4555
HCS LipidTox Green (1:1000)	Thermo Fisher	H34475
HCS LipidTox Deep Red (1:1000)	Thermo Fisher	H34477
LPDS (Lipoprotein deficient serum)	Prepared as described [52]	N/A
Bodipy 493/503	Thermo Fisher	D3922
Bodipy-C_{12} 500-510 (1:1000)	Thermo Fisher	D3822
Bodipy-C_{12} 558-568 (1:1000)	Thermo Fisher	D3835
DOPC (1,2-dioleyl-sn-3glycero-3-phosphocholine)	Avanti Polar Lipids	850375C
biotynil-DOPE (1,2-dioleyl-sn-glycero-3-phosphoetanolamine-N-(biotinyl))	Avanti Polar Lipids	870282P
Rhodamine-DOPE (1,2-dioleyl-sn-glycero-3-phosphoethanolamine-N-(lissamine rhodamine B sulfonyl)	Avanti Polar Lipids	810150P
Chloroform	Sigma	288306
Triolein	Sigma	T7140
TG-NBD (1,3-Di(cis-9-octadecenoyl-2-((6-(7-notrobenz-2-oxa-1, 3-diazol-4-yl) amino) hexanoyl) glycerol (5:1000)	Setareh Biotech	6285
Cholesteryl oleate	Sigma	C9253
SE-NBD (5-cholesten-3β-ol 12-[(7-nitro-2-1,3-benzoxadiazol-4-yl)amino]dodecanoate) (5:1000)	Avanti Polar Lipids	810252P
Bovine Serum Albumin (BSA)	Sigma Aldrich	A7906-100G

(*Continued on next page*)

Continued

REAGENT or RESOURCE	SOURCE	IDENTIFIER
Oleic acid (400μM)	Sigma Aldrich	O1008-1G
Streptavidin coated microspheres	Bangs Laboratories	CP01006
Experimental Models: Cell Lines		
A431 cells (ATCC CRL-1555, sex: female)	ATCC	CRL-1555
Cos7 cells	Dr. Marie-Françoise Bourgeade (Inserm UMR-S 1193)	N/A
HeLa cells	Laboratoire de chimie de l'Ecole Normale Supérieure de Paris	N/A
Oligonucleotides		
GL2/Ctrl siRNA, sense: CGUACGCGGAAUACUUCGA	Sigma [53]	N/A
Rab10 siRNA, target: AACTGCGTCCTTTTTCGTTTT	QIAGEN	N/A
Recombinant DNA		
pEGFP-HPos	[32]	N/A
YFP-Seipin	Dr. Mathias Beller, Heinrich-Heine Dusseldorf university	N/A
sec61β-mCherry	[54]	Addgene #49155
pEFIRES-P-HPos-mCherry	[26]	Addgene #87159
BFP-KDEL	[55]	Addgene #49150
pcDNA4/HisMaxC-RTN4	This study	N/A
pcDNA4/HisMaxC-RAB10	This study	N/A
pcDNA4/HisMaxC-ALT1	This study	N/A
pcDNA4/HisMaxB-Seipin	This study	N/A
pmCherry-C1-Climp-63	This study	N/A
pEGFP-N1-REEP5	This study	N/A
pmCherry-N1-REEP5	This study	N/A
Software and Algorithms		
Fiji	[56]	https://imagej.net/Fiji
Adobe illustrator CS4	Adobe	https://www.adobe.com
GraphPad Prism 7.0a	GraphPad	https://graphpad.com/scientific-software/prism/
CellProfiler	[57]	https://cellprofiler.org
Huygens Professional	Scientific Volume Imaging	https://svi.nl/Huygens-Professional
ilastik	[58]	https://www.ilastik.org
Other		
8-well Lab-Tek II #1.5 coverglass slides	Thermo Fisher	155409
#1.5 polymer μ-slide 8 well ibiTreat chambers	Ibidi	80826
Glass coverslips	VWR	Menzel Glasser, 631-0701
35 mm coverslip dishes	MatteK	P35G-0-20-C
Glass capillaries	W3 30-0017	Harvard Apparatus

RESOURCE AVAILABILITY

Lead Contact

Further information and requests for reagents may be directed to, and will be fulfilled by the lead contact, Abdou Rachid Thiam (thiam@ens.fr).

Materials Availability

This study did not generate new unique reagents.

Data and Code Availability

This study did not generate datasets.

EXPERIMENTAL MODEL AND SUBJECT DETAILS

Mammalian cells

A431 cells (ATCC CRL-1555, sex: female) were maintained in Dulbecco's modified Eagle's medium (DMEM) containing 10% fetal bovine serum (FBS), penicillin/streptomycin (100 U/ml each), L-glutamine (2 mM) at 37°C in 5% CO_2.

Cos7 and HeLa cells were maintained in DMEM supplemented with 10% heat inactivated FBS and 1% penicillin-streptomycin. They were cultured in 35 mm coverslip dishes (MatteK ref P35G-0-20-C) 16 h at 37°C, 5% CO_2 prior to transfection. Transfections of plasmids (Lipofectamine LTX with PLUS Reagent and X-tremeGENE 9 DNA Transfection Reagent) and siRNAs (HiPerfect) were carried out according to the manufacturer's instructions. Cells were incubated for 24 h and then imaged, or subjected to feeding or swelling experiment (detailed in the Method Details section). For feeding control experiments, cells were fed with oleic acid (Sigma Aldrich) at 400 μM conjugated to 1% bovine serum albumin solution (BSA) in DMEM during 15 min at 37°C to promote LD formation.

METHOD DETAILS

siRNAs and plasmids

Reticulon 4 (GenBank: NM_207520.1), RAB 10 (GenBank: NM_016131.4) and Atlastin 1 (GenBank: NM_001127713.1) cDNAs were amplified from A431 cDNA and inserted into pcDNA4/HisMaxC vector through restriction ligation. Seipin (GenBank: BC012140) cDNA was amplified by PCR from a plasmid kindly provided by Hongyuan Yang [18], and inserted into pcDNA4/HisMaxB. CLIMP63 (GenBank: NM_006825.3 with nucleotide 210-212 deletion) was amplified from A431 cDNA and inserted into pmCherry-C1 through restriction cloning. REEP5 (GenBank: NM_005669.5) was amplified from A431 cDNA and inserted into pEGFP-N1 or pmCherry-N1 vector through restriction cloning. Primer sequences are available upon request. BFP-KDEL cDNA (Addgene #49150) was a gift from Gia Voeltz [55]. HPos-mCherry has been described [26]. Ctrl siRNA has been described [53]. Pre-validated siRNA against Rab10 was from QIAGEN (#1027415, target sequence: ACTGCGTCCTTTTTCGTTTT). YFP-Seipin was a gift from Dr. Mathias Beller; sec61β-mCherry was purchased from Addgene (#49155) and was from the group of Gia Voeltz [54]; pEGFP-HPos was a gift form Dr. Albert Pol [32].

Stable cell lines

A431 end-miniIAA7-GFP-Sec61β cells have been described [59], these harbor miniIAA7-GFP tag at the endogenous locus of Sec61β. A431 seipin degron cells, seipin NE-trapped cells, Rab18 KO cells, end-seipin-sfGFPx7 cells expressing BFP-KDEL and LiveDrop-mCherry and end-seipin-SNAPf cells have been described [28]. Seipin-degron-A cells were used for data in Figures 2A, 6A, 6B, 6E, 6F, 6J, S6A, and S6B. Seipin-degron-B cells were used for the data in Figures 6C and 6D. To generate stable cells expressing the ER luminal marker BFP-KDEL, cells were transfected with BFP-KDEL cDNA and single clones were obtained as described in [28]. To generate stable pools overexpressing seipin, reticulon 4, atlastin 1 and Rab10, seipin-degron A cells were transfected with the respective plasmids and the expressing cell populations enriched using zeocin, pcDNA4/HisMax C alone was used as a control plasmid. Experiments were conducted 2-3 weeks after selection.

Large ER-derived Intra-Cellular vesicle experiments

For swelling experiments, Cos7 and HeLa cells were first transfected for 24 h with the indicated plasmids. The culture media of the cells was next replaced by a hypotonic culture media (DMEM:H2O 1:20). The cells were then incubated at 37°C, 5% CO2 for 5 minutes, to induce ER-vesicles. For analyzing seipin localization (Figures 1J–1L and S1A–S1C), cells were imaged directly after swelling. For Figures 2C–2I, 3, S2C–S2G, and S3 the cells were next incubated with 400 μM OA conjugated to 1% (w/w) BSA in DMEM:H2O (1:20) media at 37°C to induce LDs formation. For Figures 2C, 2D, and S2D, Bpy-C_{12} 558/568 was also added to OA (1:1000) to stain nascent LDs. Z stacks imaging of entire cells were done before and 15 min after OA administration. For Figures 3, S3A, and S3B, Bpy-C_{12} 500/510 was added to OA (1:1000) to induce and visualize nascent LDs and TG localization. Z stacks of the entire cell were imaged after swelling, before feeding, and 15 minutes after feeding. For Figure S3C, GFP-HPos is used as a marker for LDs. In all experiments where LipidTox deep red was used, it was always added in the swelling medium, before OA addition, to mark pre-existing and emerging nascent LDs, and also ER-vesicles hydrophobicity.

Delipidation, DGATi Treatments, LD Induction, seipin depletion with IAA, SNAP-labeling

Where indicated, cells were delipidated by culturing in serum-free medium supplemented with 5% lipoprotein deficient serum (LPDS). LPDS was prepared as described in [52]. Where indicated, cells were additionally incubated with DGAT1 and DGAT2 inhibitors for the final 18 h, DGATi indicates treatment with both inhibitors. To wash out DGATi, cells were washed three times with PBS and incubated in 5% LPDS medium for 5 min prior to inducing LD biogenesis with 0.2 mM OA or 0.2 mM cholesterol-cyclodextrin (final concentration) for indicated times. OA complex with BSA in 8:1 molar ratio was prepared in serum-free DMEM or FluoroBrite DMEM as described [60]. 50 mM stock of cholesterol:methyl-β-cyclodextrin complex (molar ratio 1:6.2) was prepared in H_20 by sonication. For depletion of seipin, IAA was added to the medium for 18 h, vehicle control was Milli-Q-H_2O (1:100).

Live cell analysis of LD formation sites and ER morphology

Cells were seeded onto fibronectin-coated (10 μg/ml fibronectin for 1-2 h followed by washes in PBS) 8-well Lab-Tek II #1.5 coverglass slides. Imaging was performed in Fluorobrite DMEM medium supplemented with 5% LPDS. Live cell imaging was performed with Zeiss LSM 880 confocal microscope equipped with Airyscan (Fast) detector using a 63 X Plan-Apochromat oil objective, NA 1.4, at 37°C, 5% CO_2 with incubator insert PM S1 and definite focus hardware autofocus system. Imaging was done using Airyscan super resolution ILEX-mode (Figures 1D, 2A, S1A, S1B, S2I, and 6E) or super resolution fast mode (Figures 1A and 1F), with sequential excitation of fluorophores using appropriate lasers and stable emission filter sets. The Airyscan detector was adjusted regularly between acquisitions and images were Airyscan-processed using default settings with the Zeiss Zen software package. For live cell time-lapse acquisitions, single focal planes were imaged with frame rates of 650 ms (Figure 1A), 110 ms (Figure 1F) or 30 s (Figure S2I).

For all analysis of ER morphology from live cells, BFP-KDEL channel images were segmented into background, tubules and sheets using ilastik (using pixel classification mode). For the data in Figures 1A and 1B, the nuclear envelope was also separately segmented, as some of the videos analyzed were from the relatively flat plane of ER below the nucleus. For analysis of LD formation sites marked by accumulation of LiveDrop-mCherry at seipin sites (Figures 1A and 1B), a circular region of interest (ROI) of 0.1 μm^2 in size, centered on a LD-forming seipin, was manually annotated from three frames (650 ms apart) prior to the first signs of LiveDrop accumulation. The distribution of segmented ER pixels at this ROI compared to the overall pixel distribution in the same frames was analyzed in ImageJ FIJI.

For analysis of nascent LD localization after LD formation (Figures 1D, 1E, 2A, 2B, and 6E–6I), cells were imaged as described above, imaging peripheral regions of the ER. The ER, LDs and seipins were segmented using ilastik and for each cell, the distribution of segmented ER pixels (either sheet or tubule) at either LD-associated seipins (Figures 1D, 1E, 6H, and 6I) or at LDs (Figures 2A, 2B, 6E, and 6F) was compared to the overall ER pixel distribution in the same cell, using CellProfiler and custom-made MATLAB scripts described in [28]. The localization of seipins in the ER was also analyzed in a similar manner, comparing the distribution of segmented ER pixels at seipin foci to the overall ER pixel distribution in the same cell (Figure 1G).

For analysis of ER marker protein distribution, peripheral regions of the ER were imaged as described above. ER was segmented using the BFP-KDEL channel. The mean intensity ratio of BFP-KDEL at sheets versus tubules was analyzed and compared to the mean intensity ratio of ER marker proteins (REEP-5, CLIMP-63, SEC61β) in that cell, using CellProfiler and custom-made MATLAB scripts described in [28].

LD analysis of fixed cells

Cells were seeded onto Ibidi μ-slide 8 well ibiTreat chambers. After indicated treatments, cells were washed with PBS, fixed with 4% PFA in 250 mM HEPES, pH 7.4, 100 mM$CaCl_2$ and 100 mM$MgCl_2$ for 20 min, followed by quenching in 50 mM NH_4Cl for 10 min and 3 washes with PBS. Cells were stained with DAPI and LD540 for 20 min at RT. Cells were kept in PBS and imaged within 24 h of fixation. Z stacks spanning the whole cell (step size 0.3 μm) were acquired with Nikon Eclipse Ti-E microscope, 60X PlanApo VC oil objective NA 1.4 with 1.5x zoom. Image stacks were deconvolved using Huygens batch processing application, and deconvolved image stacks were maximum intensity projected in MATLAB. Analysis of LD sizes/cell was performed as described in detail in [28], using CellProfiler and custom-made MATLAB scripts. For the data in Figures 6A and 6B, cells were immunostained with anti-Xpress (1:500) and Alexa-647 (1:400) antibodies as described [28], and fields of view with antibody staining positive cells were imaged.

DEV preparation

In vitro experiments were performed in the following HKM buffer: 50 mM HEPES, 120 mM Kacetate, and 1 mM MgCl2 (in Milli-Q water) at pH 7.4 and 275 ± 15 mOsm. All GUVs were composed of 99% DOPC (Avanti polar lipids, Inc), 0.5% (w/w) Rhodamine-DOPE, and 0.5% (w/w) biotinyl-DOPE. GUVs were prepared by electro-formation [50]. PLs and mixtures thereof in chloroform at 0.5 μM were dried on an indium tin oxide (ITO) coated glass plate. The lipid film was desiccated for 1 h. The chamber was sealed with another ITO coated glass plate. The lipids were then rehydrated with a sucrose solution (275 ± 15 mOsm). Electro-formation is performed using 100 Hz AC voltage at 1.0 to 1.4 Vpp and maintained for at least 2 h. This low voltage was used to avoid hydrolysis of water and dissolution of the titanium ions on the glass plate. GUVs were directly collected with a Pasteur pipette.

To prepare the TG artificial LDs (aLDs), 5 μL of the oil was added to 45 μL of HKM buffer. TG aLDs were composed of 99,5% triolein and 0,5% (w/w) TG-NBD. TG-SE aLDs labeled with NBD fluorescent SE were composed of 70% triolein, 29,5% (w/w) cholesteryl oleate and 0,5% (w/w) SE-NBD. TG-SE aLDs labeled with NBD fluorescent TG were 70% triolein, 29,5% (w/w) cholesteryl oleate, and 0,5% TG-NBD (w/w).

In each case, the oil/HKM buffer mixture was sonicated for 30 s in a bath sonicator to generate aLDs. To make DEVs, GUVs were incubated with the aLDs for 5 min. The GUV-aLDs mixture was then placed on a glass coverslip pretreated with 10% (w/w) BSA and washed three times with buffer. Where indicated, (Figures 5G, S5G–S5I, and S4D–S4F), Bodipy 493/503 was added to the bulk solution to label NLs.

To prepare the model membranes incorporating TG and TG-NBD (Figure S3A), we took advantage of formation giant multilamellar vesicles (GMV) during the electroformation of DOPC GUV. During the formation of DEVs, the GMVs also incorporate aLDs made of TG containing TG-NBD, as above. The GMV-aLDs mixture was then placed on a glass coverslip pretreated with 10% (w/w) BSA and washed three times with buffer. LipidTox Deep Red was then added to the buffer to analyze LipidTox fluorescence signal versus TG-NBD signal (Figure S3A).

Micromanipulation

Micro-pipettes were made from capillaries with a micropipette puller (Sutter instrument model P-2000). Micromanipulation was performed with a micromanipulator Eppendorf TransferMan 4r. Micro-pipettes were used to manipulate DEVs. The pipettes were incubated in a 5% BSA for 1 h prior to conducting experiments to prevent droplet and membrane from adherence to the glass.

Nanotube formation and radius modulation by micro aspiration

For pulling nanotubes from a DEV (or a GUV), streptavidin coated microspheres were added to the bulk on the glass coverslip. Then, the DEV was gently captured by one of the two micro-pipettes to control surface tension of the DEV (see section below). One streptavidin coated microsphere was caught by the other micro-pipette and it was slowly moved toward the DEV. Upon contact, the biotinylated phospholipid of the DEV interacted strongly to the streptavidin coated microsphere surface. Finally, a nanotube was pulled by removing slowly the micro-pipette at the opposite direction to the DEV. The radius of the tube was modulated by altering the surface tension of the DEV.

$$R_t = \sqrt{\frac{\kappa}{2\gamma}},$$

where κ is the bending rigidity of the DOPC membrane.

Nanotube radius measurements with fluorescence calibration

We vary the tube length at constant surface tension, which keeps the radius constant based on the previous equation. Therefore, for a given tension, we have many couples of tube length (L_t) and tongue length (L_p) in the micropipette (see Figure S4A). The conservation of surface yields

$$L_p = a.L_t + b.$$

Thus, from this conservation, we can extract the slope (a) by measuring different couples of L_p and L_t.

On the other hand, conservation of the volume of the system links the radius of the tube to that of the of the GUV (R_g) and the pipette through the following Equation [41]:

$$R_t = a.\left(1 - \frac{R_p}{R_g}\right).R_p$$

We measured different values of R_t, according to the above formula, and determined the associated Rh-DOPE intensity on the tube, normalized by the signal on the GUV. Thereupon, we established a calibration curve enabling us to determine the tube radius by measuring the fluorescence intensity of Rh-DOPE.

Surface tension measurements

Surface tensions were also measured. Using Laplace's law, and the measurement of the pipette inner radius (R_p), DEV (or GUV) radius (R_g), and suction pressure, the surface tension of the interface was calculated:

$$\gamma = \frac{\Delta P_{suc}}{2\left(\frac{1}{R_p} - \frac{1}{R_g}\right)},$$

where ΔP_{suc} is the suction pressure. The suction was carried out using a level of water (precision 0.005 mm). The resulting pressure was measured with the water level variation between the zero (no aspiration and no ejection of buffer) and the aspiration of a DEV tongue in the micropipette. The nanotubes were pulled and modulates by changing surface tension between 5.10^{-1} mN/m and 10^{-3}mN/m.

Tube modulation and TG distribution experiments

The oil distribution measurements in membrane nanotubes (Figure 4), were done by changing very slowly the tube radius step by step, typically every 20 s. For nucleation experiments (Figures 5E–5I and S5D–S5H), the nanotube diameter was decreased spontaneously from a value above 160 nm to values below 140 nm. For Figure 5H, the total number of nucleation events observed was counted and plotted as a function of the final nanotube radius. For Figure 5I, each time the nanotube radius was decreased drastically, it was considered as a trial, and if a nucleation event was observed, it was considered as a success event. The nucleation frequency corresponds to the number of success events divided by the number of trials.

FRAP experiments

FRAP experiments on ER-vesicles (Figure 3E) were performed on vesicles of around 10 μm in size and on their middle plane, fluorescence recovery of Bpy-C_{12} signal is normalized by the fluorescence signal in the entire vesicle. FRAP experiments on nanotubes (Figures 5A–5C) were performed by bleaching the signal on entire nanotubes (radii between 30 and 60 nm) to ensure unidirectional recovery of the fluorescence from molecules in the GUV. Planar membrane FRAP experiments on DEVs (Figures S5A–S5C) were

performed by bleaching the apex of the DEV. Rh-DOPE and TG-NBD or SE-NBD signals were bleached simultaneously. The fluorescence signal recovery was monitored. All FRAP curves are normalized by the fluorescence before bleaching GUVs and just after the bleach (in non-bleached regions). GraphPad Prism was used to fit the FRAP recovery curves with a non-linear regression and the exponential "one-phase association model."

QUANTIFICATION AND STATISTICAL ANALYSIS

Image analysis of swelling experiments and *in vitro* studies

Images were analyzed using ImageJ software. For analysis of seipin enrichment in different sized ER-derived vesicles, (Figures 1I and S1G), fluorescence profiles were drawn perpendicular to ER-derived vesicles, averaged over 10 pixels for large objects and the full size of the objects was considered when they were small. The peaks of the profiles were measured. Peak values for both YFP-seipin and sec61β-were recorded, seipin enrichment values indicate the seipin/sec61 fluorescence intensity ratio. The sizes of the analyzed vesicles were also measured and plotted. Vesicles which were below the resolution limit of the imaging setup were grouped at 0.2 μm in Figure 1J. Finally, the values were normalized so that 1 indicates the minimum seipin enrichment ratio.

For Figure 2F, LDs (stained by Bodipy-C_{12} or LipidTox deep red) in the entire cells were counted and we determined the fraction of LDs in contact with micrometric-sized vesicles (D > 1μm). We also determined the total signal of YFP-seipin and sec61β-mCherry fluorescence on submicrometric and micrometric-sized vesicles. For both category of vesicles, the number of LDs were normalized to either sec61β or seipin signal Figures 2G and 2I. In Figure 2H, YFP-seipin over sec61β-mCherry signal ratio was represented for submicrometric to micrometric-sized membrane.

For Figures 3A and 3B, a fluorescence profile was drawn perpendicular to the micrometric-sized ER-vesicles and averaged over 10 pixels. The LipidTox fluorescence intensity of the peak was recorded on ER-vesicles before OA addition and t = 15 min after OA addition on the same ER-vesicles. The values in Figure 3B are normalized by the mean value of the LipidTox fluorescence of vesicles before OA addition.

For Figures 3C and 3D, a fluorescence profile was drawn perpendicular to the micrometric-sized ER-vesicles and averaged over 10 pixels. The Bpy-C_{12} fluorescence intensity of the peak was recorded on ER-vesicles at t = 20 min and t = 35 min on the same ER-vesicles. The values in Figure 3D are normalized by the mean value of the Bpy-C_{12} fluorescence intensity of the vesicles at t = 20 min. For Figures S3E and S3F, a fluorescence profile was drawn perpendicular to the micrometric-sized ER-vesicles and the plasma membrane. It was averaged over 10 pixels. The Bpy-C_{12} and LipidTox fluorescence intensity of the peak was recorded after OA addition. The values in Figure S3F are normalized by the fluorescence intensity mean value of ER-vesicles for both LipidTox and Bpy-C_{12} signals.

For Figures S3G and S3H, a fluorescence profile was drawn perpendicular to the micrometric-sized ER-vesicles and the newly formed LDs. It was averaged over 10 pixels for the ER vesicles and 5 pixels for the LDs. The Bpy-C_{12} and LipidTox fluorescence intensity of the peak was recorded after OA addition. The values in Figure S3G are normalized by the mean value of the fluorescence intensity of ER-vesicles for both LipidTox and Bpy-C_{12} signals.

For TGs concentration analysis in ER-vesicles (Figure 3G), a fluorescence profile was drawn perpendicular to each vesicle. The maximum was taken for both Bpy-C_{12} and sec61β-mcherry. TG concentrations in the ER membrane was considered as the fluorescence ratio between Bpy-C_{12} and sec61β-mcherry. The TG concentrations in submicrometric and micrometric-sized membranes were plotted in Figure 3G and all values are normalized by the mean TG concentration in the micrometric-sized membranes. Figure 3I follows the same quantification protocol as Figures 2F and 2G.

For oil distribution measurements (Figure 4) between planar and curved membranes, a fluorescence profile was drawn perpendicular to the nanotube and averaged over several microns, the maximum of this profile which corresponds to the fluorescence of the tube was taken (for both NBD and Rhodamine) (Figure 4C). These two values are normalized by the mean fluorescence of the GUV. The oil enrichment values (Figures 4D, 4E, 4G, and 4H) corresponds to the ratio of NBD over Rhodamine fluorescence signals and are normalized by the concentration of oil in the planar membrane.

For Figure 5, the fluorescence intensity of the nanotubes and artificial nucleated droplets were recorded with a profile averaged over the size of the nucleated droplet, and normalized by the fluorescence in the DEV, for both NBD (or Bodipy) and Rhodamine signals.

Statistical analysis

Statistical comparisons where made using a non-parametric t test (GraphPad Prism; *** indicates $p < 0.0001$ ** indicates $p <$ 0,001 * indicates $p < 0.05$). Unless mentioned, all values shown in the text and Figures are mean ± SD.